

## Charge transfer driven emergent phenomena in oxide heterostructures

This content has been downloaded from IOPscience. Please scroll down to see the full text.

2017 J. Phys.: Condens. Matter 29 243001

(<http://iopscience.iop.org/0953-8984/29/24/243001>)

View [the table of contents for this issue](#), or go to the [journal homepage](#) for more

Download details:

IP Address: 202.66.60.167

This content was downloaded on 31/07/2017 at 07:05

Please note that [terms and conditions apply](#).

You may also be interested in:

[The 2016 oxide electronic materials and oxide interfaces roadmap](#)

M Lorenz, M S Ramachandra Rao, T Venkatesan et al.

[Electronic phenomena at complex oxide interfaces: insights from first principles](#)

Rossitza Pentcheva and Warren E Pickett

[Resonant elastic soft x-ray scattering](#)

J Fink, E Schierle, E Weschke et al.

[Intrinsic interfacial phenomena in manganite heterostructures](#)

C A F Vaz, F J Walker, C H Ahn et al.

[Screening mechanisms at polar oxide heterointerfaces](#)

Seungbum Hong, Serge M Nakhmanson and Dillon D Fong

[Polarity of oxide surfaces and nanostructures](#)

Jacek Goniakowski, Fabio Finocchi and Claudine Noguera

[Exotic s-wave superconductivity in alkali-doped fullerenes](#)

Yusuke Nomura, Shiro Sakai, Massimo Capone et al.

[Oxide interfaces for novel electronic applications](#)

L Bjaalie, B Himmetoglu, L Weston et al.

[Interfacial magnetism in complex oxide heterostructures probed by neutrons and x-rays](#)

Yaohua Liu and Xianglin Ke

## Topical Review

# Charge transfer driven emergent phenomena in oxide heterostructures

Hanghui Chen<sup>1,2,4</sup> and Andrew Millis<sup>3</sup><sup>1</sup> NYU-ECNU Institute of Physics, New York University Shanghai, 200062, People's Republic of China<sup>2</sup> Department of Physics, New York University, New York, NY 10002, United States of America<sup>3</sup> Department of Physics, Columbia University, New York, NY 10027, United States of AmericaE-mail: [hanghui.chen@nyu.edu](mailto:hanghui.chen@nyu.edu)

Received 21 April 2016, revised 6 April 2017

Accepted for publication 24 April 2017

Published 18 May 2017

**Abstract**

Complex oxides exhibit many intriguing phenomena, including metal-insulator transition, ferroelectricity/multiferroicity, colossal magnetoresistance and high transition temperature superconductivity. Advances in epitaxial thin film growth techniques enable us to combine different complex oxides with atomic precision and form an oxide heterostructure. Recent theoretical and experimental work has shown that charge transfer across oxide interfaces generally occurs and leads to a great diversity of emergent interfacial properties which are not exhibited by bulk constituents. In this report, we review mechanisms and physical consequence of charge transfer across interfaces in oxide heterostructures. Both theoretical proposals and experimental measurements of various oxide heterostructures are discussed and compared. We also review the theoretical methods that are used to calculate charge transfer across oxide interfaces and discuss the success and challenges in theory. Finally, we present a summary and perspectives for future research.

Keywords: transition metal oxides, first-principles calculations, strong correlation

(Some figures may appear in colour only in the online journal)

**1. Introduction**

Artificial oxide heterostructures can now be grown with atomic precision [1]. At oxide interfaces, charge transfer is a very general and robust phenomenon. With electrons moving from one oxide to the other, new charge configurations can be induced at the interface. These charge configurations can be substantially different from those found in bulk versions of the constituent materials. As a consequence, at oxide interfaces new electronic, magnetic and orbital states emerge. A classical example of emergent phenomena in oxide heterostructures is the  $\text{LaAlO}_3/\text{SrTiO}_3$  interface [2], where a high mobility two-dimensional electron gas exhibiting magnetism and superconductivity is discovered at the interface [3–8], while both  $\text{LaAlO}_3$  and  $\text{SrTiO}_3$  are wide band gap insulators.

During the past decade, designing new oxide heterostructures and seeking new interfacial phenomena have been a focus of condensed matter physics [9–11]. The exciting new discoveries pose a challenge for theory: can we reliably describe and predict charge transfer phenomena in oxide heterostructures, in particular when constituting oxides are strongly correlated?

In this report, we discuss charge transfer effects at oxide interfaces. We first distinguish three important mechanisms of charge transfer in oxide heterostructures: (1) polarity difference; (2) occupancy difference and (3) electronegativity difference. For the first two mechanisms, we briefly discuss representative examples since excellent reviews are already available [1, 12–14]. We focus on the last mechanism and present a comprehensive review of various examples and different emergent phenomena arising from interfacial charge transfer. Next we briefly describe theoretical methods that are widely used in literature to calculate charge transfer in oxide

<sup>4</sup> Author to whom any correspondence should be addressed.

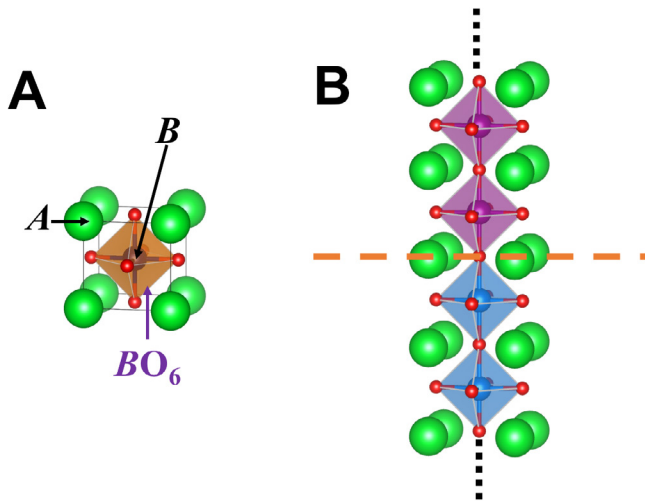


**Figure 1.** (A) Atomic structure of a perovskite oxide (the formula unit is  $ABO_3$ ). (B) Two different transition metal oxides are stacked along the  $[001]$  direction. The orange dashed line highlights the interface.

heterstructures and discuss the theoretical challenges pertinent to descriptions of charge transfer in strongly correlated materials. Finally we present a summary and our perspectives for the field of oxide heterostructures. Space limitations and the rapid development of the field mean that the review can not be comprehensive. We apologize to those whose work is not included here.

In this review we focus on an important class of transition metal oxides: perovskite oxides. Their atomic structure is shown in figure 1(A). The atom on the corner of the cube is called *A*-site atom, which is either an alkaline earth metal or a rare earth metal. The atom at the center of the cube is called *B*-site atom, which is a transition metal. Each transition metal atom is surrounded by six oxygen atoms which are at face-center of the cube. As we form an oxide heterostructure using two perovskite oxides, we need to choose a stacking direction. In this review, unless otherwise specified, we focus on  $(001)$  interfaces, which are shown in figure 1(B).

## 2. Overview of charge-transfer mechanisms

The materials separated by an interface will generically have different electronic properties, and therefore different chemical potentials (measured, say, relative to the vacuum level) and this difference will generally lead to charge flow across the interface. With the transferred electrons, the physical and chemical properties of the constituent oxides close to the interface can be fundamentally different from bulk properties because the transition metal *d* occupancy is changed.

In the context of oxide interfaces, it is useful to distinguish three driving mechanisms, all of which contribute to the chemical potential difference: polarity difference, occupancy difference and electronegativity difference. The classification of different charge transfer mechanisms is not unambiguous. In fact, different mechanisms are closely related and sometimes intertwined. The classification is nonetheless useful, because charge transfer across oxide interfaces always occurs

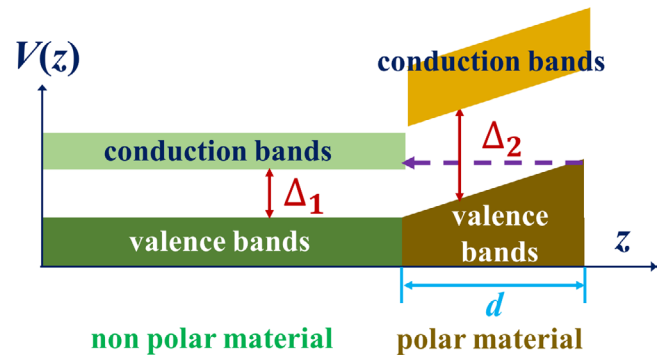


**Figure 2.** Potential profile of an ideal interface (i.e. no band misalignment) between a nonpolar material and a polar material.  $\Delta_1$  ( $\Delta_2$ ) is the band gap of the nonpolar (polar) material.  $d$  is the thickness of the polar material. In the polar material, an average internal polar field  $\frac{dV}{dz} = E$  exists. The dashed arrow shows the charge transfer when the thickness  $d$  is above the critical value (defined in equation (1) in the main text).

to compensate for some type of ‘discontinuity’, and our classification lists the three most relevant types.

### 2.1. Polarity difference

In this review, a polar material is understood as an insulator (polar metals have recently been experimentally synthesized [15, 16], which however goes beyond the scope of our current discussion) such that along a certain direction, in the form of a stoichiometric thin film, an average internal electric field develops. Correspondingly, a nonpolar material is an insulator such that in the stoichiometric thin film, along the given direction, the internal electric field is averaged to zero. For example, stoichiometric  $(001)$   $\text{LaAlO}_3$  films are polar because they are composed of alternating  $(\text{LaO})^{+1}$  and  $(\text{AlO}_2)^{-1}$  layers, while stoichiometric  $(001)$   $\text{SrTiO}_3$  films are nonpolar since they consist of alternating  $(\text{SrO})^0$  and  $(\text{TiO}_2)^0$  layers. However, we note that along the  $(110)$  direction,  $\text{SrTiO}_3$  can be considered as polar because of the alternating  $(\text{SrTiO})^{4+}$  and  $(\text{O}_2)^{4-}$  layers.

We focus on  $[001]$  as the stacking direction. Figure 2 illustrates the interface between a polar material and a nonpolar material. An average internal polar field  $E = \frac{dV}{dz}$  is developed in the polar material along the  $[001]$  direction. The potential difference between one side of the polar material and the other side is proportional to the thickness of the material  $d$ . Therefore as

$$eEd > \min\{\Delta_1, \Delta_2\} \quad (1)$$

electrons can tunnel from the surface to the interface ( $\Delta_1$  is the band gap of the nonpolar material and  $\Delta_2$  is the band gap of the polar material). As a consequence of charge transfer, electrons emerge in the conduction bands of the nonpolar material (if  $\Delta_1 < \Delta_2$ ) or in the conduction bands of the polar material (if  $\Delta_1 > \Delta_2$ ) and holes appear in the valence band of the polar material (on the surface). The smallest value of  $d$  that satisfies equation (1) defines the critical thickness. For the *n*-type  $\text{LaAlO}_3/\text{SrTiO}_3$  interface (the interface with  $\text{LaO}/\text{TiO}_2$

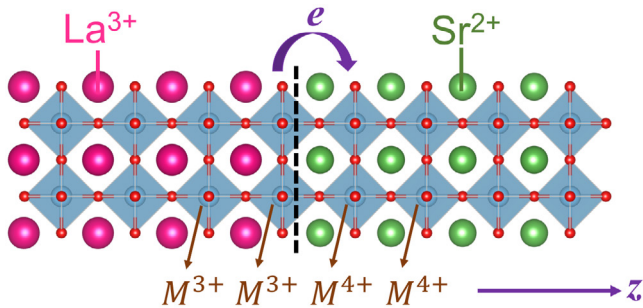


**Figure 3.** Atomic structure of the interface between  $\text{LaMO}_3$  and  $\text{SrMO}_3$  where  $M$  is a transition metal ion. In  $\text{LaMO}_3$ , the formal valence of  $M$  is  $3+$ , while in  $\text{SrMO}_3$ , the formal valence of  $M$  is  $4+$ . The purple arrow indicates that electrons may transfer from  $M^{3+}$  to  $M^{4+}$  at the interface.

terminations), the experimental critical thickness is 4 unit cells [3]. As  $d$  is above the critical thickness, the two-dimensional electron/hole gas at the interface and surface counteracts the internal field in the polar material. The sheet density of electrons/holes increases with the thickness  $d$  of the polar material and approaches the saturation value as  $1/d$  when the internal polar field is completely compensated [17–19].

However, we need to make two important comments:

- (1) we note that equation (1) is based on the assumption that valence bands are perfectly aligned. If there is a significant band misalignment between the polar and the nonpolar materials, equation (1) needs to be refined. However, the general picture that charge transfers from one side of the polar material to the other side above a critical thickness remains qualitatively the same.
- (2) the polar catastrophe mechanism provides one way to compensate the internal polar field. However, as the thickness  $d$  of the polar material is large enough (in the limit of bulk materials), other compensation mechanism will be in play, such as vacancies, interstitials and adsorbed molecules. The  $\frac{1}{d}$  thickness dependence of sheet carrier density only applies to the situation without defect formation.

## 2.2. Occupancy difference

The second mechanism is the difference of transition metal  $d$  occupancy across the interface. Many transition metal ions, such as Ti, V and Mn, have multiple valences and the valence state can be controlled by other elements in a compound. For example, in  $\text{ABO}_3$  perovskite materials, one may think of the O ions as having formal valence  $2^-$ , while the A ion may have formal valence  $2^+$  (if  $A = \text{Sr}, \text{Ca}, \text{Ba}$ , etc) or  $3^+$  (if  $A = \text{La}$  or other member of the lanthanide series), so charge neutrality fixes the valence of the B-site transition metal ions as  $4^+$  (if  $A = \text{Sr}$ ) or  $3^+$  (if  $A = \text{La}$ ). While formal valence is an oversimplification of the true situation, it provides a useful description. Figure 3 illustrates the interface between  $\text{LaMO}_3$  and  $\text{SrMO}_3$ . Without charge transfer, the formal valence of transition metal ion  $M$  abruptly changes from  $3+$  to  $4+$  at the interface. This discontinuity drives a charge flow, so that some

electrons on  $M^{3+}$  ions may flow to  $M^{4+}$  ions, which smooths out the occupancy discontinuity at the interface. However, we note that difference in transition metal  $d$  occupancy does not always lead to charge transfer, or even if charge transfer does occur, conduction does not necessarily emerge at the interface. This is ascribed to the competition between correlation effects and kinetic energies. We will discuss it in more details in subsequent sections.

## 2.3. Electronegativity difference

The third mechanism is the difference in electronegativity of dissimilar transition metals  $M$ . Loosely speaking, electronegativity (or sometimes referred to as electron affinity) is a measure of the energy gain (or cost) of moving an electron from a reservoir to the ion in question; of course the value of the electronegativity depends on the choice of reservoir and on the valence of the ion. The electronegativity, defined at constant valence, decreases as one moves from left to right across the transition metal series and the differences in electronegativity play an important role in the magnitude of the charge transfer. As a rough rule of thumb, we observe that the greater the electronegativity difference, the greater the magnitude of the charge transfer. To make these considerations more specific and quantitative, we first remark that in transition metal oxides, one may think of the  $\text{O}^{2-}$  as providing the reservoir. Thus the electronegativity is in essence the energy separation between transition metal  $d$  and oxygen  $p$  states, which is often referred to as the charge transfer energy [20]. In many oxide superlattices, the oxygen states approximately align across the interface so that the electronegativity difference translates directly into a contribution to the chemical potential difference and can drive charge transfer, as shown in figure 4(A). This figure shows the interface between  $\text{AMO}_3$  and  $\text{AM}'\text{O}_3$ , where the two transition metal ions  $M$  and  $M'$  have identical formal valences (i.e. no polar discontinuity), but have different energy levels of their  $d$  states (different electronegativity) as shown in figure 4(B), leading to transfer of electrons from  $M$  to  $M'$  across the interface to reduce the total energy.

We note that similar to the previous discussion, we perfectly align the O  $p$  states across the oxide interface in figure 4, which is an oversimplification: although the oxygen states form a continuous network the energies do not exactly align across interfaces. However, the simplified picture provides a very useful way of understanding the results of detailed calculations.

## 3. Polarity difference (polar catastrophe)

The charge transfer mechanism of polarity difference at oxide interfaces is commonly known as the ‘polar catastrophe’. The term becomes commonly used after Ohtomo and Hwang synthesized  $\text{LaAlO}_3$  thin films of a few unit cells thick on  $\text{SrTiO}_3$  substrates with a  $\text{TiO}_2$  termination and discovered a high-mobility electron gas at the  $\text{LaAlO}_3/\text{SrTiO}_3$  interface [2]. While the  $\text{LaAlO}_3/\text{SrTiO}_3$  interface (to be more precise, the one with  $\text{LaO}/\text{TiO}_2$  termination, sometimes referred to as

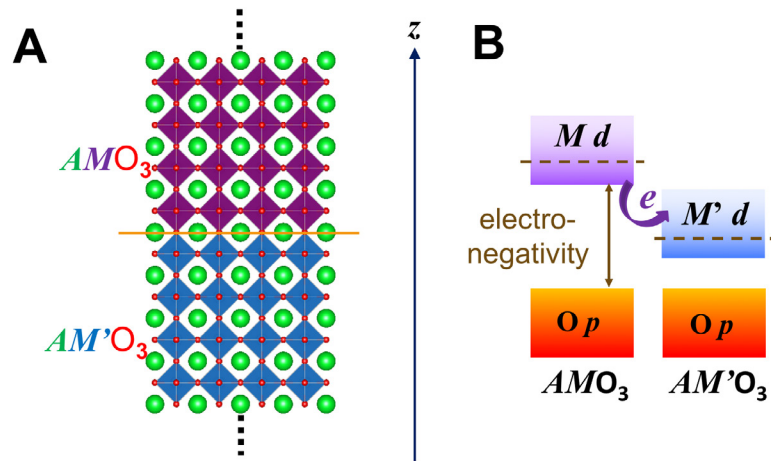


**Figure 4.** (A) Atomic structure of the interface between  $AMO_3$  and  $AM'O_3$ . (B) Schematics of band alignments of  $d$  states of transition metal  $M$  and  $M'$  as well as oxygen  $p$  states. The solid arrow indicates the energy difference between metal  $d$  states and oxygen  $p$  states, a measure of electronegativity of transition metal  $M$ . If the  $d$  states of transition metal  $M$  have higher energy than those of  $M'$ , electrons can transfer from  $M$  to  $M'$  across the interface.

the  $n$ -type interface) is just one example of the ‘polar catastrophe’ mechanism [21], it is an important special case which has stimulated numerous theoretical and experimental works, and led to many unexpected phenomena including magnetism [5, 7, 8], superconductivity [4, 6] and tunable Rashba spin-orbital interaction [22, 23]. We refer readers to the excellent review papers that have already appeared in literature [1, 12–14].

However, we want to comment that while the  $LaAlO_3/SrTiO_3$  interface is the prototype of the ‘polar catastrophe’ mechanism, accumulating evidence shows that the ‘polar catastrophe’ mechanism alone can not explain all the observed experimental results. For example, early experiments failed to observe the average internal polar field in  $LaAlO_3$  [24]. Later experiments do report an internal polar field, but the magnitude is only  $80 \text{ meV } \text{\AA}^{-1}$  [25], smaller than the first-principles calculations by at least a factor of 2 [26, 17]. This implies that in addition to charge transfer, other mechanisms can also screen the internal polar field, leading to smaller values than theoretical predictions. Recently a polarity-induced defect mechanism was proposed to account for both conduction and magnetism at the  $LaAlO_3/SrTiO_3$  interface [27]. Chambers *et al* [28] show that at the (001)  $LaCrO_3/SrTiO_3$  interface, a potential gradient within the polar material  $LaCrO_3$  is sufficient to trigger a charge transfer, which one would expect to lead to conduction. However, the interface is experimentally found to be insulating. The insulating behavior is attributed to cation-intermixture.

All these results show that at a general polar-nonpolar interface, the ‘polar catastrophe’ picture which is based on the *ideal* atomic structure probably is not the only mechanism in play. Atomic reconstruction, such as cation intermixture, various types of vacancies and point defects, are very likely to occur.

#### 4. Occupancy difference

The charge transfer mechanism of occupancy difference between oxide interfaces are closely related to the ‘polar catastrophe’ mechanism. However, we use this classification

to refer to one particular type of superlattices which have been under intensive study. The general formula of those superlattices can be expressed as  $RMO_3/AMO_3$  where  $R$  is a tri-valent cation,  $A$  is a di-valent cation and  $M$  is a transition metal ion. The most common case for  $R$  is La and for  $A$  is Sr. Important examples of these oxide heterostructures include  $LaTiO_3/SrTiO_3$  [29, 30],  $LaMnO_3/SrMnO_3$  [31, 32] and  $LaVO_3/SrVO_3$  [33, 34] superlattices.

Like the  $LaAlO_3/SrTiO_3$  interface, there are also many reviews in literature discussing  $LaTiO_3/SrTiO_3$ ,  $LaMnO_3/SrMnO_3$  and related oxide heterostructures [14]. Here we briefly review these important examples and mention some points that from our perspective deserve attention for future research.

The authors of [29] show that as a few unit cells of Mott insulator  $LaTiO_3$  are embedded into a band insulator  $SrTiO_3$  matrix, electrons move from the Ti atoms in  $LaTiO_3$  to the Ti atoms in  $SrTiO_3$ , providing emergent conduction at the interface. Similar phenomena have also been reported for a few unit cells of Mott insulating  $GdTiO_3$  embedded into an  $SrTiO_3$  matrix. The carrier concentration at this interface is even higher [35]. Okamoto and Millis [30] show that charge transfer and conduction are general features at the interface between a semi-infinite Mott insulator and a semi-infinite band insulator. However, if we change the geometry, different phenomena can emerge. Jang *et al* [36] shows that if we insert only a single  $RO$  layer in a  $SrTiO_3$  matrix, and if  $R = La, Pr$  and  $Nd$ , conduction appears at the interface, but if  $R = Sm$  and  $Y$ , the interface remains insulating. References [37, 38] study another related geometry: they consider inserting  $SrO$  in a Mott insulator  $GdTiO_3$  matrix and both theory and experiment find that due to extreme quantum confinement, a dimer Mott insulating state can be stabilized.

The second example is  $(LaMnO_3)_m/(SrMnO_3)_n$  superlattices with different Sr/La ratio (by varying  $m$  and  $n$ ). An important case is that  $m = 2n$ , which deserves special attention [39]. For  $(LaMnO_3)_{2n}/(SrMnO_3)_n$  superlattices, as  $n$  increases from 1 to 5, a metal-insulator transition occurs (for  $n \leq 2$ , the interface is metallic and for  $n \geq 3$ , the interface becomes insulating)

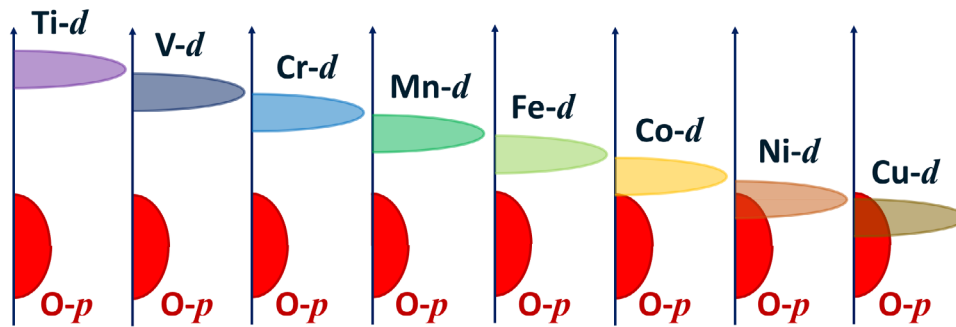


**Figure 5.** Schematics of energy levels of transition metal  $d$  states with respect to oxygen  $p$  states in transition metal oxides  $\text{LaMO}_3$  ( $M = \text{Ti, V, Cr, Mn, Fe, Co, Ni}$  and  $\text{Cu}$ ). As the mass of transition metal elements increases, the metal  $d$  level decreases. For titanates,  $\text{Ti-}d$  states lie above  $\text{O-}p$  by about 3 eV. For nickelates and cuprates,  $\text{Ni-}d$  and  $\text{Cu-}d$  states even lie below  $\text{O-}p$  states, leading to a ‘negative charge transfer’ energy and strong hybridization.

[40]. For the nature of insulating states, authors of [40] suggest that a finite peak does exist in the density of states at the Fermi level but it is localized by disorder. A recent experiment [31] proposes that it is the quantum fluctuation that disrupts the coherence of metallic states, giving rise to the insulating properties observed in  $n \geq 3$  superlattices. However, theoretical work [41, 42] shows that within a reasonable range of parameters, the ideal interface between semi-infinite  $\text{LaMnO}_3$  and semi-infinite  $\text{SrMnO}_3$  should be metallic.

In [33] the authors synthesize  $(\text{LaVO}_3)_m/(\text{SrVO}_3)_1$  superlattices ( $m$  varies from 2 to 6) and find that the superlattices have a net magnetization up to room temperatures due to the geometrically confined doping. However, the authors of [34, 43] show theoretically that the experimentally determined crystal structure of  $\text{LaVO}_3/\text{SrVO}_3$  superlattices is not favorable to induce ferromagnetism. They propose that large amplitude of oxygen octahedral rotations would be needed to stabilize a ferromagnetic state.

We note that for these  $(\text{LaMO}_3)_m/(\text{SrMO}_3)_n$  superlattices (where  $M = \text{Ti, Mn}$  and  $\text{V}$ ), their chemical composition is equivalent to  $\text{La}_{1-x}\text{Sr}_x\text{MO}_3$  where  $x = \frac{n}{m+n}$  and  $0 < x < 1$ . The physical properties of solid solution  $\text{La}_{1-x}\text{Sr}_x\text{MO}_3$  have also been comprehensively investigated in theory and experiment [44, 45]. For  $x = 0$  or 1, the end material is usually insulating (band insulator or Mott insulator). In the solid solution ( $0 < x < 1$ ), conduction emerges within a range of  $x$ . However, as we have seen from the above examples, with the same chemical composition, the superlattices can exhibit distinct properties from solid solutions. For examples, solid solution  $\text{La}_{2/3}\text{Sr}_{1/3}\text{MnO}_3$  is ferromagnetic metallic but  $(\text{LaMnO}_3)_{10}/(\text{SrMnO}_3)_5$  superlattice is insulating.  $(\text{LaVO}_3)_6/(\text{SrVO}_3)_1$  superlattice exhibits a large magnetic moment of  $1.4 \mu_B/\text{V}$  ion, whereas solid solution  $\text{La}_{6/7}\text{Sr}_{1/7}\text{VO}_3$  shows a much smaller net magnetization. Another important difference of superlattices from compositionally equivalent solid solutions is the anisotropy of transport. While solid solutions usually show three dimensional conduction, the emergent conduction in superlattices is confined to interfaces and exhibits two dimensional character, which may be more useful for device development.

We also need to mention that in many systems, both charge occupancy difference and polarity effects will contribute to

the charge transfer. The  $\text{LaAlO}_3/\text{SrTiO}_3$  and  $\text{LaTiO}_3/\text{SrTiO}_3$  [29],  $\text{GdTiO}_3/\text{SrTiO}_3$  [46] systems provide useful examples. In the former, the Al valence is the same in all layers and the charge transfer depends strongly on the thickness of the polar  $\text{LaAlO}_3$  layers, becoming negligible for less than 4 unit cells, so here the charge transfer is entirely driven by polarization effects. In the latter systems the amount of charge transfer depends on the thickness of polar  $\text{LaTiO}_3$  (or  $\text{GdTiO}_3$ ) layers but does not vanish even for 1 monolayer. Furthermore, the near interface Ti ions in the  $\text{LaTiO}_3$  (or  $\text{GdTiO}_3$ ) have a valence different from that of the Ti farther from the interface; thus both mechanisms contribute in this system.

## 5. Electronegativity difference

In this section, we present a detailed review of electronegativity-driven charge transfer in oxide heterostructures. We focus on the following interfaces  $\text{AMO}_3/\text{AM}'\text{O}_3$  or double perovskite  $\text{A}_2\text{MM}'\text{O}_6$ , where  $A$  is di-valent or tri-valent ion and  $M, M'$  are dissimilar transition metal ions. Figure 5 schematically shows the energy separation between metal  $d$  and oxygen  $p$  states for 3d transition metal oxides  $\text{LaMO}_3$  ( $M = \text{Ti, V, Cr, Mn, Fe, Co, Ni}$  and  $\text{Cu}$ ). We note that as the mass of transition metal element increases, the Coulomb attraction to the nucleus lowers the energy of transition metal  $d$  states, so the electronegativity increases as one moves from left to right along the transition metal row. For titanates, the energy separation between  $\text{Ti-}d$  and  $\text{O-}p$  states is about 3 eV. However, for nickelates and cuprates, the  $\text{Ni-}d$  and  $\text{Cu-}d$  states lie even below the  $\text{O-}p$  states, which leads to a ‘negative charge transfer’ energy and strong hybridization between metal  $d$  and oxygen  $p$  states. The electronegativity-driven charge transfer is based on the energy difference between the  $d$  states of two different transition metal ions.

Before we move on, we note that an electronegativity difference does not always drive charge transfer. If one material  $\text{AMO}_3$  is a wide gap insulator with a nominally empty  $M-d$  shell and the  $d$  states of  $M$  ions lie above those of  $M'$  ions, then no charge transfer occurs between  $M$  and  $M'$  ions.  $\text{SrTiO}_3/\text{SrVO}_3$  is one example in which there is no charge transfer between  $\text{SrTiO}_3$  and  $\text{SrVO}_3$  [47].  $\text{LaAlO}_3/\text{LaNiO}_3$  is another

example [48]. This situation is called quantum confinement which reduces the band width of transition metal ions and also leads to emergent phenomena, but it goes beyond the scope of our current paper and we refer the readers to other review papers [49].

### 5.1. $\text{LaTiO}_3/\text{LaNiO}_3$ and $\text{LaTiO}_3/\text{LaNiO}_3/\text{insulator}$ superlattices

We start from the interface between  $\text{LaTiO}_3$  and  $\text{LaNiO}_3$ . Bulk  $\text{LaTiO}_3$  is an antiferromagnetic  $S = 1$  Mott insulator with a nominal  $d^1$  occupancy on Ti atoms. Bulk  $\text{LaNiO}_3$  is a paramagnetic metal with a nominal  $d^7$  occupancy on Ni atoms. As figure 6(A) shows, in bulk  $\text{LaTiO}_3$ , Ti- $d$  states lie above O- $p$  states by about 3 eV, while in bulk  $\text{LaNiO}_3$ , Ni- $d$  states have strong hybridization with O- $p$  states. In a  $\text{LaTiO}_3/\text{LaNiO}_3$  superlattice with a short periodicity, the lone electron on Ti- $d$  states is expected to transfer to Ni- $d$  states. Therefore after the charge transfer, in the superlattice Ti atoms nominally have a  $d^0$  occupancy and Ni atoms nominally have a  $d^8$  occupancy. In the new charge configuration, as figure 6(B) shows, Ti atoms have an empty  $d$  shell; Ni atoms have a full  $t_{2g}$  shell and a half-filled  $e_g$  shell. If the correlation strength on Ni sites is strong enough, a Mott gap will open up. In this way, by design, we can induce an artificial Mott insulating state via a nominally complete charge transfer from Ti to Ni in  $\text{LaTiO}_3/\text{LaNiO}_3$  superlattices [50]. Figure 6(C) presents the theoretically calculated density of states for  $(\text{LaTiO}_3)_1/(\text{LaNiO}_3)_1$  superlattices, as compared to the density of states for the classical Mott insulator NiO (in which Ni atoms also nominally have a  $d^8$  occupancy) as well as bulk  $\text{LaNiO}_3$  and  $\text{LaTiO}_3$ . We can see that the Ti- $d$  conduction bands, which are partially filled in bulk  $\text{LaTiO}_3$ , become completely empty in the  $(\text{LaTiO}_3)_1/(\text{LaNiO}_3)_1$  superlattice. On the other hand, the Ni- $d$  states, which are partially filled in bulk  $\text{LaNiO}_3$ , are filled up in the  $(\text{LaTiO}_3)_1/(\text{LaNiO}_3)_1$  superlattice. As a consequence, a gap is opened in the superlattice, which separates Ni- $d$  and Ti- $d$  states. The lower and upper Hubbard bands of Ni- $d$  states in the superlattice are very similar to those in NiO, which is a strong evidence of the charge-transfer-driven Mott insulating state on Ni sites.

Inspired by the theoretical predictions in [50], Cao *et al* [51] synthesized a  $(\text{LaTiO}_3)_2/(\text{LaNiO}_3)_2$  superlattice and measured the transport properties. Figure 7(A) shows the atomic structure of the superlattice. Figure 7(B) shows the temperature dependence of sheet resistance of  $(\text{LaTiO}_3)_2/(\text{LaNiO}_3)_2$  superlattice and  $\text{LaNiO}_3$  film. The former is highly insulating while the latter exhibits metallic behavior. To probe the change in charge states, figures 7(C) and (D) show the Ti  $L_{2,3}$  and Ni  $L_2$  edge of  $(\text{LaTiO}_3)_2/(\text{LaNiO}_3)_2$  superlattices measured by the x-ray absorption spectroscopy. Panel (C) shows that the formal valence of Ti in the superlattice changes from the value 3+ in bulk  $\text{LaTiO}_3$  to 4+ as in  $\text{SrTiO}_3$ , while the formal valence of Ni in the superlattice changes from the value 3+ in bulk  $\text{LaNiO}_3$  to 2+ as in NiO. These results are consistent with the theoretical predictions in [50] and provide convincing evidence of charge transfer in the  $(\text{LaTiO}_3)_2/(\text{LaNiO}_3)_2$  superlattices.

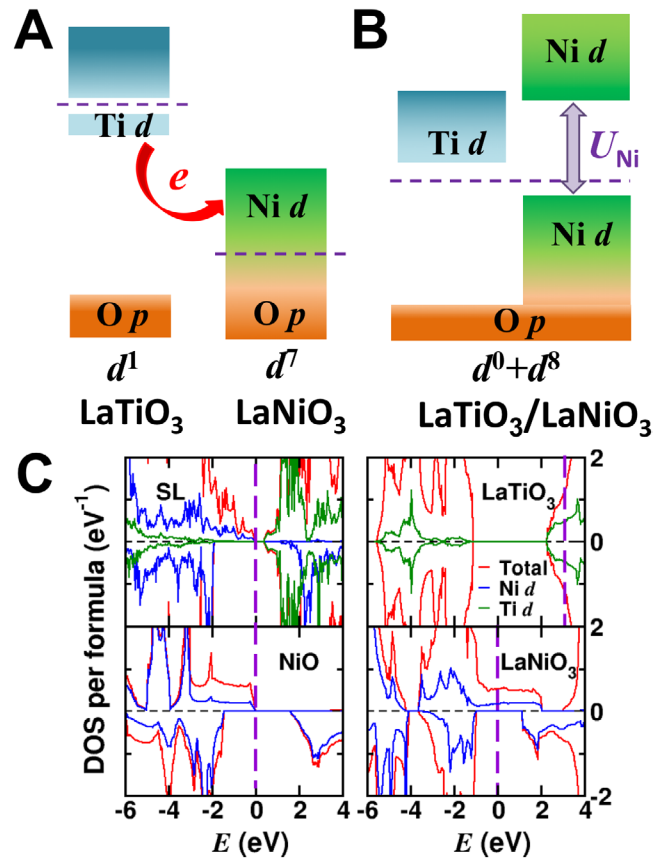


**Figure 6.** (A) Schematic band structures of component materials  $\text{LaTiO}_3$  and  $\text{LaNiO}_3$ . The dashed purple lines are the Fermi levels for the two materials.  $\text{LaTiO}_3$  shows insulating behavior with a small excitation gap set by Ti  $d$ - $d$  transitions and a wide energy separation between Ti  $d$  states and O  $p$  states.  $\text{LaNiO}_3$  exhibits metallic behavior with strong mixing between Ni  $d$  states and O  $p$  states. The red arrow highlights the direction of charge transfer in the superlattice. (B) Schematic band structure of  $(\text{LaTiO}_3)_1/(\text{LaNiO}_3)_1$  superlattice. Ti  $d$  states are above the Fermi level (dashed purple line). Correlation effects split Ni  $d$  states into lower and upper Hubbard bands, separated by  $U_{\text{Ni}}$ . (C) Densities of states for majority (above axis) and minority (below axis) spins of superlattice (upper left) and reference materials NiO (lower left),  $\text{LaTiO}_3$  (upper right); zero of energy is shifted so that oxygen bands align with those of  $\text{LaNiO}_3$  and  $\text{LaNiO}_3$  (lower right). The densities of states are obtained using DFT +  $U$  calculations with  $U_{\text{Ni}} = 6$  eV and  $U_{\text{Ti}} = 4$  eV. Reprinted with permission from [50]. Copyright (2013) by the American Physical Society.

In addition to the charge transfer from Ti to Ni across the interface between titanates and nickelates, Grisolia *et al* [52] find a more subtle effect. By synthesizing and comparing  $\text{GdTiO}_3/\text{RNiO}_3$  interfaces ( $R = \text{La, Nd, Sm}$ ), they find that the magnitude of charge transfer from Ti to Ni can be tuned by the element  $R$ . The charge transfer increases from  $\text{LaNiO}_3$  to  $\text{NdNiO}_3$  to  $\text{SmNiO}_3$ . The underlying mechanism is that different ionic sizes of  $R$  affect the oxygen octahedral rotations and thus hybridization between Ni- $d$  and O- $p$  states. Because what we for simplicity refer to as the  $d$ -state is an antibonding  $p$ - $d$  hybrid, the  $p$ - $d$  covalency affects the energy. Therefore, in addition to the energy gain by moving electrons from Ti- $d$  states of higher energies to Ni- $d$  states of lower energies, Ni- $d$  and O- $p$  states change their hybridization and covalent character (so-called ‘rehybridization’), which also costs energy.

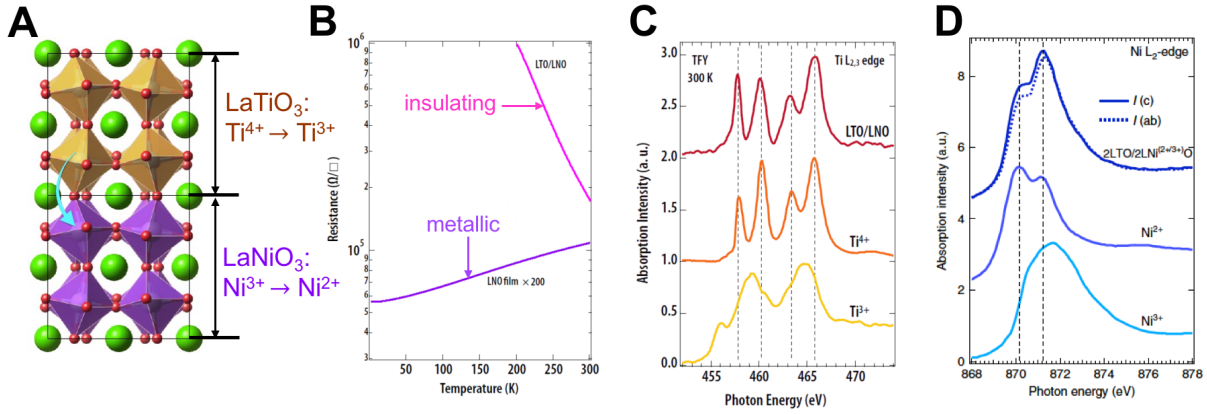


**Figure 7.** (A) Atomic structure of  $(\text{LaTiO}_3)_2/(\text{LaNiO}_3)_2$  superlattices. (B) Temperature-dependent sheet resistances of the  $(\text{LaTiO}_3)_2/(\text{LaNiO}_3)_2$  superlattices and the reference  $\text{LaNiO}_3$  film (20 unit cells). It is noteworthy that the sheet resistance of  $\text{LaNiO}_3$  film is  $\times 200$ . (C) and (D) X-ray absorption spectroscopy (XAS) of  $(\text{LaTiO}_3)_2/(\text{LaNiO}_3)_2$  superlattices. (C)  $\text{Ti } L_{2,3}$ -edge. The reference spectra for  $\text{Ti}^{4+}$  and  $\text{Ti}^{3+}$  were measured on a  $\text{SrTi}^{4+}\text{O}_3$  single crystal and  $\text{YTi}^{3+}\text{O}_3$  film ( $\sim 100$  nm on  $\text{TbScO}_3$  substrate), respectively. (D)  $\text{Ni } L_{2,3}$ -edge. The reference samples are bulk  $\text{Ni}^{2+}\text{O}$  and  $\text{LaNi}^{3+}\text{O}_3$ . Out-of-plane ( $I(c)$ , dark blue solid line,  $E \parallel c$  and  $E$  is the linear polarization vector of the photon) and in-plane ( $I(ab)$ , dark blue dashed line,  $E \parallel ab$ ) linearly polarized x-ray were used to measure XAS of  $(\text{LaTiO}_3)_2/(\text{LaNiO}_3)_2$  superlattices at  $\text{Ni } L_{2,3}$ -edge. Black dashed lines are guidelines for peak positions. All spectra were collected and repeated more than two times with bulk-sensitive total fluorescence yield (TFY) detection mode at room temperature. Adapted from [51]. CC BY 4.0.

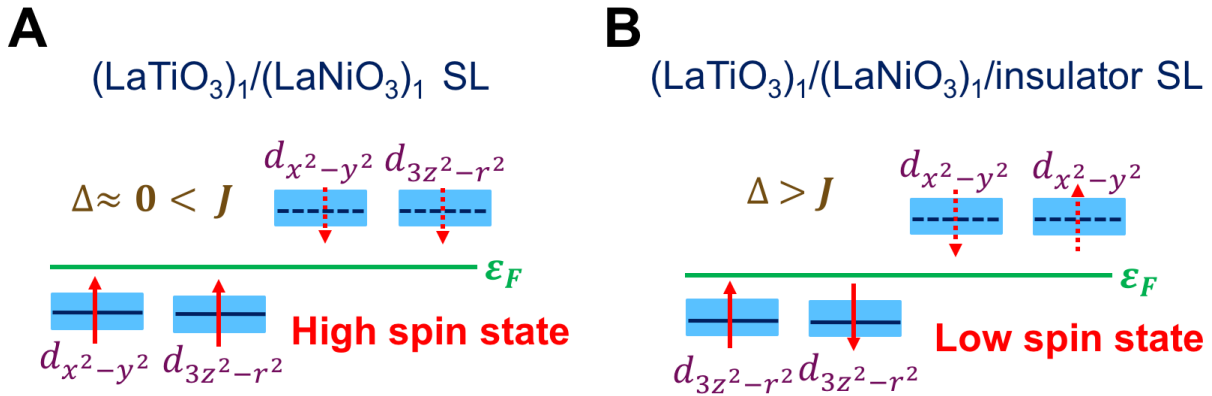


**Figure 8.** Charge and spin configurations of (A)  $(\text{LaTiO}_3)_1/(\text{LaNiO}_3)_1$  superlattice and (B)  $(\text{LaTiO}_3)_1/(\text{LaNiO}_3)_1/\text{insulator}$  superlattice.  $J$  is Hund's coupling for  $\text{Ni } d$  states and  $\Delta$  is the orbital splitting between  $\text{Ni } d_{x^2-y^2}$  and  $d_{3z^2-r^2}$  orbitals.  $\epsilon_F$  is the Fermi level. The shallow blue patches illustrate band widths and the dark blue solid/dashed line highlight the central positions of bands. As  $\Delta < J$ , the two electrons fill two different orbitals with the same spin, leading to a  $S = 1$  high-spin state. As  $\Delta > J$ , the two electrons fill the same orbital with opposite spins, leading to a  $S = 0$  low-spin state.

The larger the ionic size, the more energy the rehybridization costs, which limits the amount of charge that can be transferred across the interface. It is noteworthy [52] that while hybridization in  $R\text{NiO}_3$  tunes the charge transfer from  $\text{Ti}$  to  $\text{Ni}$  across the interface between  $\text{GdTiO}_3$  and  $R\text{NiO}_3$ , hybridization in  $R\text{TiO}_3$  plays a much less significant effect on the charge transfer across the interface between  $R\text{TiO}_3$  and  $\text{LaNiO}_3$ . The reason is that different from strong hybridization between  $\text{Ni}-d$  and  $\text{O}-p$  states, in titanates  $\text{Ti}-d$  states lie above  $\text{O}-p$  states by about 3 eV, which results in a much weaker hybridization between  $\text{Ti}-d$  and  $\text{O}-p$  states. Therefore, changing the ionic size of  $R$  in  $R\text{TiO}_3$  can not significantly tune the hybridization and therefore does not have the controlling effects on charge transfer as eminent as it does in  $R\text{NiO}_3$ .

Next we discuss a  $\text{LaTiO}_3/\text{LaNiO}_3/\text{insulator}$  tri-component superlattice [53]. The motivation of designing such a new superlattice is to engineer an unprecedented orbital state in  $\text{Ni}$  atoms (in addition to the change in charge states) [54, 55].

As in the  $\text{LaTiO}_3/\text{LaNiO}_3$  superlattice, nominally one electron transfers from  $\text{Ti}$  to  $\text{Ni}$  in the tri-color superlattice, which leads to a  $\text{Ni } d^8$  occupancy with a full  $t_{2g}$  shell and two electrons in the  $e_g$  shell. However, they have fundamental difference. As figure 8 shows, in the  $\text{LaTiO}_3/\text{LaNiO}_3$  superlattice, the two electrons in the  $\text{Ni } e_g$  shell form a high-spin  $S = 1$  state, while in the tri-component superlattice, the two electron in the  $\text{Ni } e_g$  shell form a low-spin  $S = 0$  state. The high-spin/low-spin configuration is determined by the competition between Hund's coupling  $J$  and crystal field splitting  $\Delta$ , which is the energy difference between  $\text{Ni } d_{x^2-y^2}$  and  $d_{3z^2-r^2}$  orbitals. If  $\Delta < J$ , the two electrons fill two different orbitals with the same spin, leading to a high-spin state. If  $\Delta > J$ , the two electrons fill the same orbital with opposite spins, leading to a low-spin state. The significance of a low-spin state in  $\text{Ni}$ -based oxide heterostructures is that further electron doping of the tri-component superlattice can induce a single-orbital Fermi surface, analogous to that of superconducting cuprates.

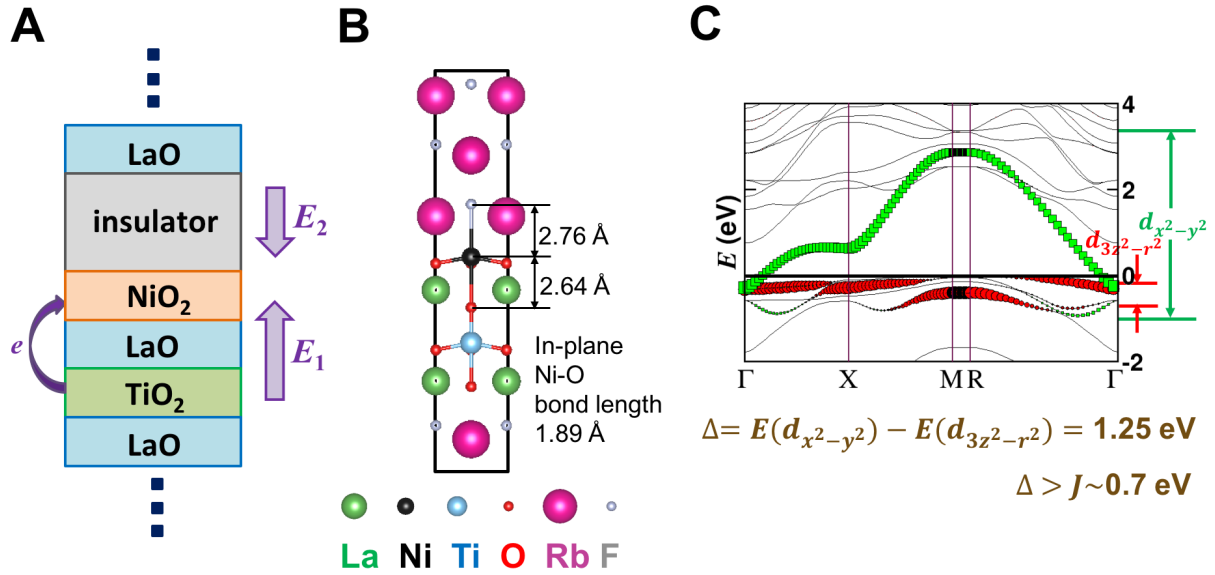


**Figure 9.** (A) Schematics of  $\text{LaNiO}_3/\text{LaTiO}_3/\text{insulator}$  superlattices. (B) Theoretically calculated atomic structure of  $(\text{LaNiO}_3)_1/(\text{LaTiO}_3)_1/(\text{RbF})_3$  superlattices. The in-plane Ni-O bond length is 1.89 Å. The out-of-plane Ni-O and Ni-F bond lengths are 2.64 and 2.76 Å. (C) Band structure of  $(\text{LaNiO}_3)_1/(\text{LaTiO}_3)_1/(\text{RbF})_3$  superlattice. The red symbols are band projections onto Ni  $d_{3z^2-r^2}$  orbital. The green symbols are band projections onto Ni  $d_{x^2-y^2}$  orbital. Using the Wannier functions to fit the DFT-calculated band structure, the difference between the on-site energy for Ni  $d_{3z^2-r^2}$  orbital and the on-site energy for Ni  $d_{x^2-y^2}$  orbital is found to be 1.25 eV. Hund's coupling for Ni  $d$  orbital is about 0.7 eV.

The orbital splitting  $\Delta$  between  $d_{x^2-y^2}$  and  $d_{3z^2-r^2}$  orbitals is induced by a Jahn–Teller-like distortion, i.e. elongation of out-of-plane Ni–O bonds. Such a structural distortion occurs to the tri-component superlattice by the combination of charge transfer and insertion of a wide-gap insulator. Figure 9(A) shows the schematics of a  $(\text{LaTiO}_3)_1/(\text{LaNiO}_3)_1/\text{insulator}$  tri-component superlattice. Charge transfer from Ti to Ni induces an internal electric field  $E_1$  and due to the periodic boundary condition a second electric field  $E_2$  appears. Both  $E_1$  and  $E_2$  pull the apical oxygen atoms away from the Ni atom, which leads to Jahn–Teller-like distortions that favor the occupancy of Ni  $d_{x^2-y^2}$  orbital over the  $d_{3z^2-r^2}$  orbital. The presence of a wide gap insulator explicitly breaks the inversion-symmetry and leads to  $E_1 \neq E_2$ . This asymmetry induces a polar distortion on Ni atoms, i.e. Ni and O are not co-planar, which further increases the out-of-plane Ni–O bond length. Figure 9(B) shows the theoretically calculated atomic structure of  $(\text{LaTiO}_3)_1/(\text{LaNiO}_3)_1/(\text{RbF})_3$  superlattices. We note that the out-of-plane Ni–O and Ni–F bond lengths are on average equal to 2.7 Å, which is much longer than the in-plane Ni–O bond length 1.89 Å. The ferroelectric-like Ni–O displacement is clearly visible. Figure 9(C) shows the band structure of  $(\text{LaTiO}_3)_1/(\text{LaNiO}_3)_1/(\text{RbF})_3$  superlattice. The red symbols are band projections onto Ni  $d_{3z^2-r^2}$  orbital. The green symbols are band projections onto Ni  $d_{x^2-y^2}$  orbital. The Ni  $d_{x^2-y^2}$  band is almost completely filled up while the Ni  $d_{3z^2-r^2}$  band is nearly empty. This confirms that the tri-component superlattice indeed has a low-spin configuration (two electrons fill the same orbital with opposite spins). On the other hand, using the maximally localized Wannier functions and fitting them to the DFT-calculated band structure, the difference  $\Delta$  between the onsite energy for Ni  $d_{3z^2-r^2}$  orbital

and that for Ni  $d_{x^2-y^2}$  orbital is calculated to be 1.25 eV. The Hund's coupling  $J$  for Ni  $d$  orbital is about 0.7 eV. Therefore it is  $\Delta > J$ , which is consistent with the low-spin configuration.

Following the theoretical proposal of [53], Disa *et al* [56] synthesized an artificial  $(\text{LaTiO}_3)_1/(\text{LaNiO}_3)_1/(\text{LaAlO}_3)_3$  superlattice and used x-ray linear dichroism (XLD) to probe the orbital occupancy. Figure 10(A) shows the experimental setup and figure 10(B) shows the orbital selective atomic transitions probed by the x-rays. The experiments compared  $\text{LaNiO}_3/\text{LaAlO}_3$  superlattice (two-component superlattice) and the tri-component superlattice. The resulting orbital-polarization-dependent spectra are shown in figures 10(C) and (D). In the two-component superlattice, no significant dichroic signal is observed (panel (C)). The red (absorption for Ni  $d_{3z^2-r^2}$  orbital) and blue (absorption for Ni  $d_{x^2-y^2}$  orbital) symbols almost overlap with each other. In contrast, there is a marked dichroism for the tri-component superlattice (panel (D)). This result represents the largest experimentally observed Ni  $e_g$  orbital polarization in perovskite nickelate systems to date. Furthermore, the Ni  $e_g$  orbital occupancy measured experimentally is in good agreement with first-principles DFT calculations. However, Fabbris *et al* [57] measured resonant inelastic x-ray scattering (RIXS) spectra for this superlattice recently and obtained good fits to the spectra by using a  $d$ -only model, i.e. we consider  $dd$  excitations from a Ni  $d^8$  atom without explicitly including oxygen  $p$  states. The fits give an on-site energy splitting between the two Ni  $e_g$  orbital of only about 0.2 eV in the superlattice, whereas a  $d$ -only Wannier function analysis of the DFT-calculated band structure gives an on-site splitting of about 0.8 eV [56]. This discrepancy, along with the fact that the  $d$ -only RIXS does yield the predicted orbital polarization, has been attributed to the hybridization between Ni  $d$  and O  $p$  states [57]. We believe

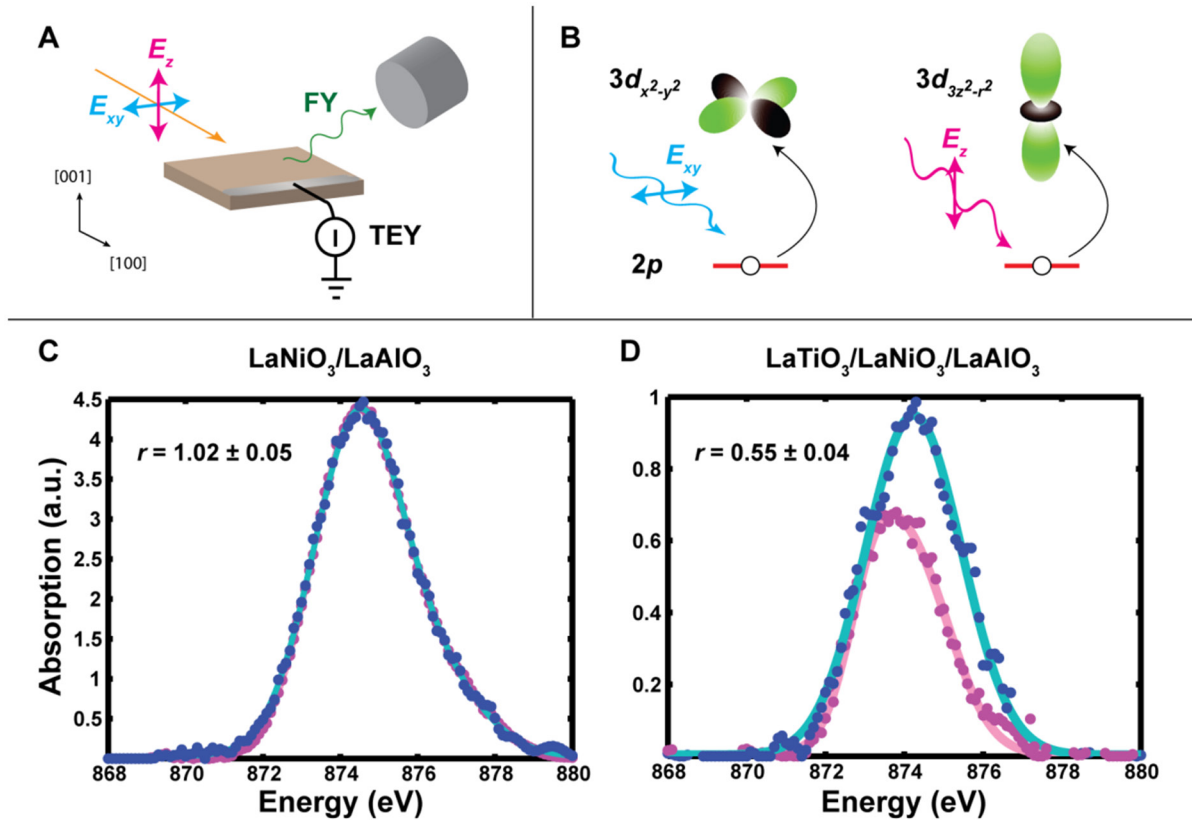


**Figure 10.** Large orbital polarization in three-component superlattices observed by x-ray linear dichroism. (A) Schematic of the experiment. (B) The orbital selective atomic transitions probed by x-ray linear dichroism. (C) Measured x-ray absorption (circles) for in-plane (blue) and out-of-plane (pink) polarizations for a two-component and (D) three-component nickelate superlattice. The solid colored lines are double Gaussian fits. Adapted with permission from [56]. Copyright (2015) by the American Physical Society.

that the  $d$ -only Wannier functions which are used to fit the DFT band structure treat  $p$ - $d$  hybridization in a different manner from the  $d$ -only RIXS model. Nevertheless, both the DFT calculations and the experimental spectra (XLD and RIXS) find a large orbital polarization in the  $(\text{LaTiO}_3)_1/(\text{LaNiO}_3)_1/(\text{LaAlO}_3)_3$  superlattice. Further work is needed to address these remaining issues.

### 5.2. $\text{LaTiO}_3/\text{LaFeO}_3$ and $\text{YTiO}_3/\text{YFeO}_3$ superlattices

$\text{LaTiO}_3/\text{LaFeO}_3$  and  $\text{YTiO}_3/\text{YFeO}_3$  superlattices are another example of a nominally complete charge transfer from Ti to Fe. The two superlattices share similarities but also have important differences.

Bulk  $\text{LaFeO}_3$  ( $\text{YFeO}_3$ ) nominally has a  $\text{Fe } d^5$  occupancy. The half-filled  $\text{Fe } d$  shell forms a high-spin state. Bulk  $\text{LaTiO}_3$  ( $\text{YTiO}_3$ ) nominally has a  $\text{Ti } d^1$  occupancy. Kleibecker *et al* [58] shows both in theory and in experiment that Ti atoms nominally donate one electron to Fe atoms across the  $\text{LaTiO}_3/\text{LaFeO}_3$  interface and after the charge transfer Fe atoms nominally have a  $d^6$  occupancy but a high-spin to low-spin transition occurs and the six electrons completely fill the  $\text{Fe } t_{2g}$  shell. Figure 11(A) illustrates such a charge-transfer-driven spin transition. The theoretically calculated density of states shows an empty  $\text{Ti } t_{2g}$  shell and a fully occupied  $\text{Fe } t_{2g}$  shell. Experimentally, by using x-ray photoelectron spectroscopy, the authors of [58] confirmed the rearrangement of the  $\text{Fe } 3d$

bands and revealed an unprecedented charge transfer up to  $1.2 \pm 0.2e^-$  per interface unit cell in the  $\text{LaTiO}_3/\text{LaFeO}_3$  heterostructures. In  $\text{YTiO}_3/\text{YFeO}_3$  superlattices, a similar charge transfer from Ti to Fe is also found in theory [59]. However, in contrast to the  $\text{LaTiO}_3/\text{LaFeO}_3$  superlattices, a robust high-spin state is found in the  $\text{YTiO}_3/\text{YFeO}_3$  superlattices, probably due to the small ionic size of Y which leads to a smaller bandwidth of  $\text{Fe } d$  states and favors the high-spin configuration. In addition to the high-spin state, hybrid ferroelectricity with a polarization  $P \sim 1 \mu\text{C cm}^{-2}$  is induced in a  $(\text{YTiO}_3)_2/(\text{YFeO}_3)_2$  superlattice. Figure 11(B) shows the atomic structure of  $(\text{YTiO}_3)_n/(\text{YFeO}_3)_n$  superlattices ( $n = 1$  and 2) with arrow highlighting the displacement of Y atoms. If  $n = 1$ , all the Y atoms have the same environment. If  $n = 2$ , there are three types of Y atoms: one is sandwiched between  $\text{TiO}_6$  and  $\text{FeO}_6$ , one is sandwiched between two  $\text{TiO}_6$  and one is sandwiched between two  $\text{FeO}_6$ . The displacements of all three types of Y atoms do not exactly cancel each other, which leads to a net polarization.

We note that in [58, 60], the authors align the valence band edge of O-2p and find the occupied  $\text{Ti } t_{2g}$  states have overlap with the empty upper Hubbard bands of  $\text{Fe } d$  states in the energy window. However, in [59], the authors align the localized O-2s states and find the occupied  $\text{Ti } t_{2g}$  states lie between the occupied lower Hubbard bands and the unoccupied upper Hubbard bands of  $\text{Fe } d$  states. However, in the calculations of both superlattices, charge transfer occurs from Ti to Fe atoms.

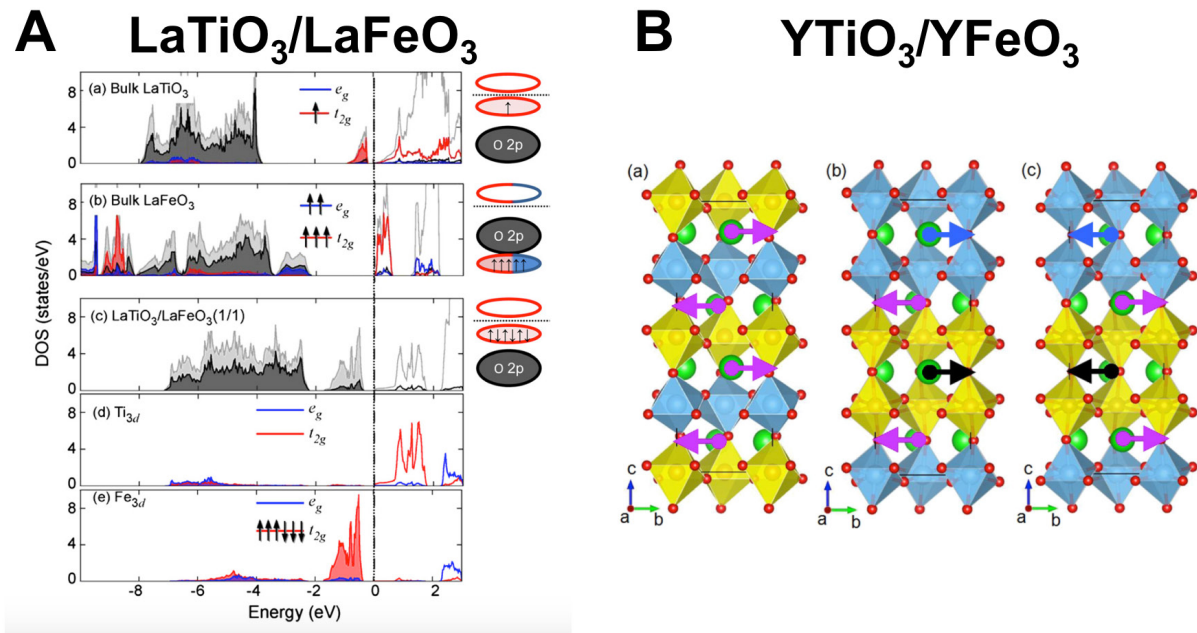


**Figure 11.** (A) Atomic and orbital projected density of states as well as schematic band structure of (a) bulk LaTiO<sub>3</sub>, (b) bulk LaFeO<sub>3</sub>, and (c)–(e) (LaTiO<sub>3</sub>)<sub>1</sub>/(LaFeO<sub>3</sub>)<sub>1</sub> superlattice. Total states are marked in gray, O *p* states in black, Fe and Ti *t*<sub>2g</sub> states in red, and Fe and Ti *e*<sub>g</sub> states in blue. The Fermi level is indicated by the dotted line. (B) Atomic structure of (YTioO<sub>3</sub>)<sub>*n*</sub>/(YFeO<sub>3</sub>)<sub>*n*</sub> superlattice (*n* = 1 and 2). Sketch of ferroelectric distortions. The arrows denote the displacements of Y<sup>3+</sup>. (a) *n* = 1. The displacements are compensated between layers. The (b) positive and (c) negative ferroelectric distortion for *n* = 2. Adapted with permission from [58] and [59]. Copyright (2014) and (2015) by the American Physical Society, respectively.

This shows that the rigid band alignment using the bulk band structures can only serve as an approximate guide. Charge transfer and the resulting band alignment at oxide interfaces should be determined in a self-consistent way, as performed in superlattice calculations.

### 5.3. LaMnO<sub>3</sub>/LaNiO<sub>3</sub> superlattices

Next we discuss the LaMnO<sub>3</sub>/LaNiO<sub>3</sub> superlattice. This is an interesting case, since up till now there is inconsistency between theory and experiment. While both theory and experiment indicate that charge transfer from Mn to Ni occurs due to electronegativity differences, experimental transport and optical measurements show that (LaMnO<sub>3</sub>)<sub>2</sub>/(LaNiO<sub>3</sub>)<sub>2</sub> superlattices are insulating [61, 62] but theoretical calculations find that the (LaMnO<sub>3</sub>)<sub>*m*</sub>/(LaNiO<sub>3</sub>)<sub>*n*</sub> superlattices with different Mn/Ni ratios *m/n* are all metallic [63].

Figure 12(A) shows the transport properties of (LaMnO<sub>3</sub>)<sub>2</sub>/(LaNiO<sub>3</sub>)<sub>*n*</sub> superlattices. As *n* decreases from 5 to 2, a metal-insulator transition occurs. In particular, in experiment the (LaMnO<sub>3</sub>)<sub>2</sub>/(LaNiO<sub>3</sub>)<sub>*n*</sub> superlattice exhibits strong insulating behavior. Figure 12(B) shows the optical conductivity of (LaMnO<sub>3</sub>)<sub>*n*</sub>/(LaNiO<sub>3</sub>)<sub>*n*</sub> as a function of *n*, temperature and frequency. Similar to transport measurements, the low frequency optical conductivity substantially drops as *n* decreases from 5 to 2. In both [61] and [62], the authors ascribe the observed metal-insulator transition to the charge transfer from Mn to Ni. Such a charge transfer is confirmed in first-principles calculations [63]. However, for both (LaMnO<sub>3</sub>)<sub>1</sub>/(LaNiO<sub>3</sub>)<sub>1</sub> and (LaMnO<sub>3</sub>)<sub>2</sub>/(LaNiO<sub>3</sub>)<sub>2</sub>, no insulating state is stabilized in the calculations. Tuning the Hubbard *U* for Mn and Ni *d* orbitals in a reasonable range does not change the metallic

properties of the superlattice. This raises the question whether the charge transfer from Mn to Ni is a nominally complete charge transfer or not. If it is, then presumably a Mott insulating state should emerge in (LaMnO<sub>3</sub>)<sub>1</sub>/(LaNiO<sub>3</sub>)<sub>1</sub> superlattice where Mn atoms have a half-filled *t*<sub>2g</sub> shell and Ni atoms have a full *t*<sub>2g</sub> and half-filled *e*<sub>g</sub> shell, similar to (LaTiO<sub>3</sub>)<sub>1</sub>/(LaNiO<sub>3</sub>)<sub>1</sub> superlattice. However, theoretical calculations show that a partial charge transfer from Mn to Ni occurs and the superlattice remains metallic. We note that double perovskite La<sub>2</sub>MnNiO<sub>6</sub> is found to be a ferromagnetic insulator in both theory [64] and experiment [65, 66]. The inconsistency between theory and experiment on LaMnO<sub>3</sub>/LaNiO<sub>3</sub> superlattices implies that the interface may not be atomically sharp and disorder such as antisite defects [67] could play a role in inducing the insulating state. Further research, in particular characterization of interfacial atomic structure using high-resolution electron microscopy, may help to resolve the problem.

We note here that for LaMnO<sub>3</sub>/LaNiO<sub>3</sub> interfaces, in addition to (001) stacking direction, (111) interfaces have also been synthesized and studied [68, 69]. Gibert *et al* [68] shows that at (111) LaMnO<sub>3</sub>/LaNiO<sub>3</sub> interface, in addition to charge transfer, exchange bias emerges, which implies the development of interface-induced magnetism in the paramagnetic LaNiO<sub>3</sub> layers. Such a bias does not show up at the (001) LaMnO<sub>3</sub>/LaNiO<sub>3</sub> interface.

### 5.4. Ba<sub>2</sub>VFeO<sub>6</sub>, Pb<sub>2</sub>VFeO<sub>6</sub> and Sr<sub>2</sub>VFeO<sub>6</sub> double perovskite oxides

Substantial charge transfer not only occurs to atomically sharp interfaces in superlattices, but also in double perovskite oxides which are bulk compounds that are based on two

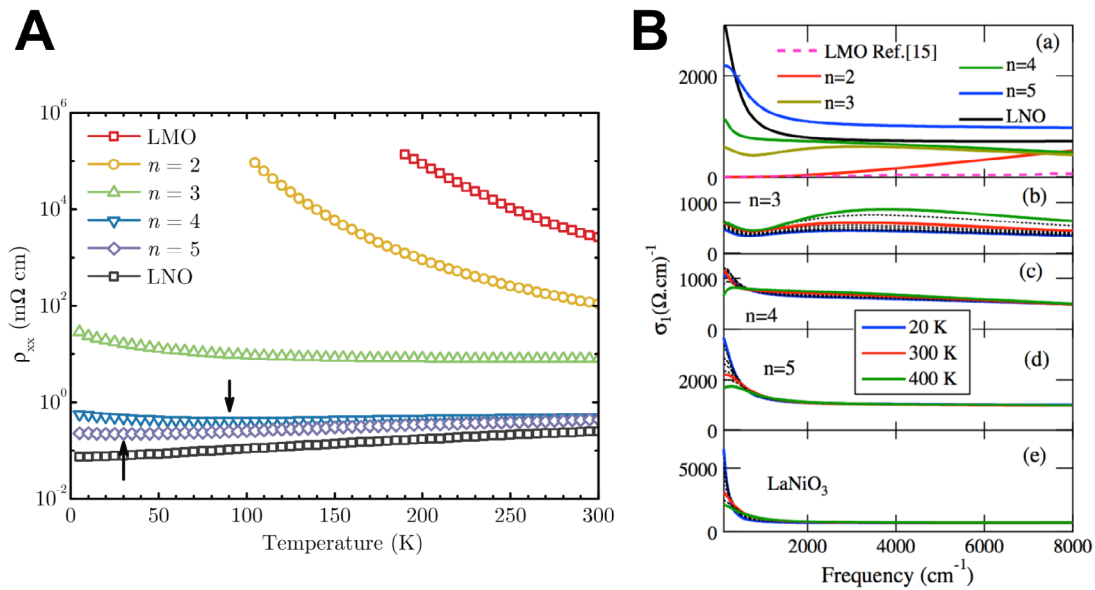


**Figure 12.** (A): Transport properties of  $(\text{LaNiO}_3)_n/(\text{LaMnO}_3)_2$  superlattices ( $2 \leq n \leq 5$ ). Temperature dependence of longitudinal resistivity  $\rho_{xx}$ . The arrows indicate positions of the resistivity minima at  $T = 90 \text{ K}$  ( $n = 4$ ) and  $T = 30 \text{ K}$  ( $n = 5$ ). (B) Optical conductivity of the  $(\text{LaNiO}_3)_n/(\text{LaMnO}_3)_2$  superlattices as extracted from a Lorentz–Drude fitting. (a) Room temperature optical conductivities of the  $n = 2, 3, 4, 5$  samples and pure  $\text{LaNiO}_3$  and  $\text{LaMnO}_3$ . (b) Temperature dependence of the optical conductivity of the  $n = 3$  compound. (c)–(e) Same for the  $n = 4, 5$  and for pure  $\text{LaNiO}_3$ . Adapted with permission from [61] and [62]. Copyright (2013) and (2015) by the American Physical Society, respectively.

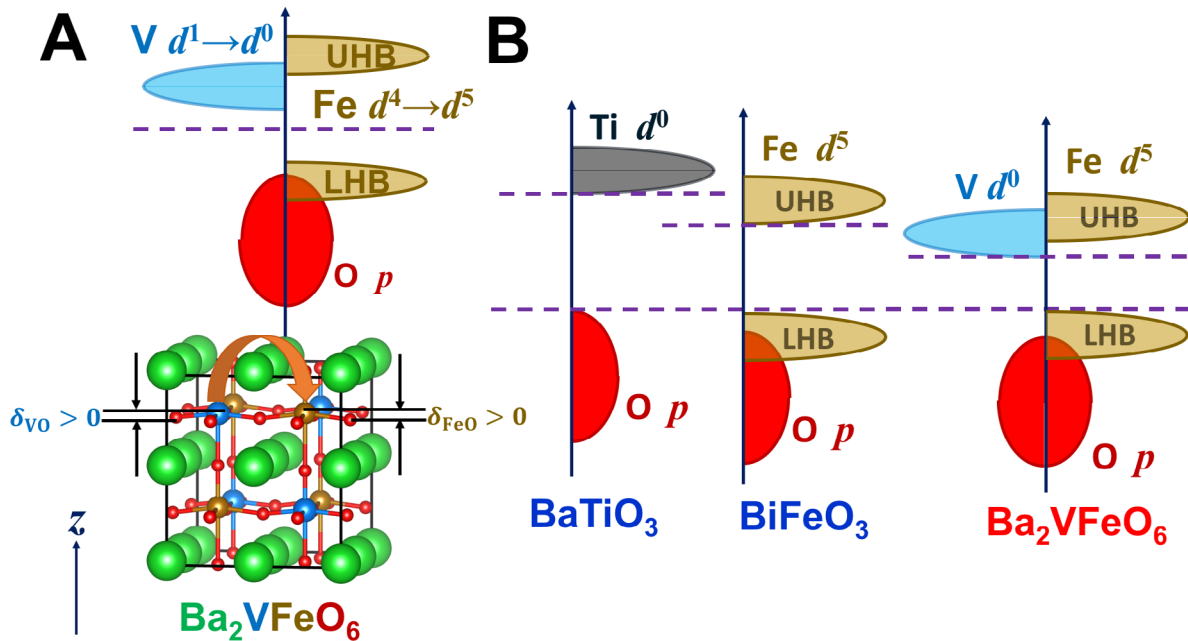


**Figure 13.** (A) Energy diagram and atomic structure of double perovskite  $\text{Ba}_2\text{VFeO}_6$ . The dashed line is the Fermi level, which lies in the gap between  $V d$  and  $Fe d$  states. LHB (UHB) means lower Hubbard bands (upper Hubbard bands). The red arrow indicates the charge transfer from  $V$  atoms to  $Fe$  atoms due to electronegativity difference. In the double perovskite  $\text{Ba}_2\text{VFeO}_6$ , a polar distortion is developed ( $\delta_{\text{VO}} > 0$  and  $\delta_{\text{FeO}} > 0$ ) because of the new charge configuration  $V d^0$  and  $Fe d^5$ . (B) Comparison of gaps for perovskite oxides:  $\text{BaTiO}_3$ ,  $\text{BiFeO}_3$  and  $\text{Ba}_2\text{VFeO}_6$ . The valence band edges are aligned for comparison.

single perovskite oxides (see figure 13 for the atomic structure). Double perovskite  $\text{Ba}_2\text{VFeO}_6$  is one example in which a nominally complete transfer from  $V$  to  $Fe$  leads to Mott multiferroic properties which do not exhibit in either bulk  $\text{BaVO}_3$  or bulk  $\text{BaFeO}_3$ . Perovskite  $\text{BaVO}_3$  crystallizes in cubic structure with a nominally  $V d^1$  occupancy. Perovskite  $\text{BaFeO}_3$  also crystallizes in cubic structure with a nominally  $Fe d^4$

occupancy. As figure 13(A) shows, in the double perovskite  $\text{Ba}_2\text{VFeO}_6$ , a nominally complete charge transfer leads to new charge configurations  $V d^0$  and  $Fe d^5$ . Since  $Fe$  atoms have a half-filled configuration, strong correlation is expected to open a Mott gap. At sufficiently low temperatures, the large local magnetic moment  $S = 5/2$  on  $Fe$  atoms is expected to order magnetically. More importantly, both the empty  $V d$

shell and the half-filled Fe  $d$  shell have a ferroelectric instability, just like the Ti  $d^0$  state in BaTiO<sub>3</sub> and the Fe  $d^5$  state in BiFeO<sub>3</sub>. The presence of Ba ions which have a large ionic size creates favorable conditions for ferroelectricity [70]. Figure 13(B) compares the band structure of BaTiO<sub>3</sub>, BiFeO<sub>3</sub> and Ba<sub>2</sub>VFeO<sub>6</sub>. In BaTiO<sub>3</sub> and Ba<sub>2</sub>VFeO<sub>6</sub>, both Ti and V have  $d^0$  occupancy. However, due to the electronegativity difference between Ti and V, the Ti  $d$  states lie above the V  $d$  states, which leads to a smaller band gap for Ba<sub>2</sub>VFeO<sub>6</sub> than for BaTiO<sub>3</sub>. On the other hand, in both BiFeO<sub>3</sub> and Ba<sub>2</sub>VFeO<sub>6</sub>, the Fe atoms have a  $d^5$  state. However, in Ba<sub>2</sub>VFeO<sub>6</sub>, we have an empty V  $d$  shell. Injecting one electron on V atoms changes its  $d$  occupancy from  $d^0$  to  $d^1$ , which does not involve correlation effects. Injecting one electron on Fe atoms changes its  $d$  occupancy from  $d^5$  to  $d^6$ , which increases the number of electron pairs and each additional pair is associated with a Hubbard  $U$  energy. Therefore the V  $d^0$  state is expected to lie below the upper Hubbard band of Fe  $d$  state, which means a smaller gap for Ba<sub>2</sub>VFeO<sub>6</sub> than for BiFeO<sub>3</sub>.

Chen and Millis [71] use first-principles calculations to support the above picture. In particular, the authors find that the polarization of Ba<sub>2</sub>VFeO<sub>6</sub> is comparable to that of BaTiO<sub>3</sub> and the gap of Ba<sub>2</sub>VFeO<sub>6</sub> is smaller than that of BaTiO<sub>3</sub> by about 1 eV. Since the experimental optical gap of BaTiO<sub>3</sub> is 3.2 eV, it is predicted that the optical gap of Ba<sub>2</sub>VFeO<sub>6</sub> is around 2.2 eV, which is 0.5 eV smaller than the optical gap of BiFeO<sub>3</sub>. This makes Ba<sub>2</sub>VFeO<sub>6</sub> a promising candidate among perovskite oxides for bulk photovoltaic applications.

In addition to Ba<sub>2</sub>VFeO<sub>6</sub>, double perovskite Pb<sub>2</sub>VFeO<sub>6</sub> has a ferroelectric polarization comparable to PbTiO<sub>3</sub>. Double perovskite Sr<sub>2</sub>VFeO<sub>6</sub>, like SrTiO<sub>3</sub>, is paraelectric but in the vicinity of ferroelectric-paraelectric phase boundary. We note that in terms of ferroelectric properties, A<sub>2</sub>VFeO<sub>6</sub> has a simple one-to-one correspondence to ATiO<sub>3</sub> ( $A = \text{Ba, Pb, Sr}$ ).

### 5.5. SrVO<sub>3</sub>/SrMnO<sub>3</sub> and Sr<sub>2</sub>VO<sub>4</sub>/Sr<sub>2</sub>MnO<sub>4</sub> superlattices

In addition to the cases of nominally ‘complete’ charge transfer (the formal valence of cation changes by  $\pm 1$ ) that are reviewed above, we may also have partial charge transfer, if the electronegativity difference between two similar transition metals is moderate. Partial charge transfer generically leads to emergent metallic properties due to the non-integer filling of bands. The authors of [72] study SrVO<sub>3</sub>/SrMnO<sub>3</sub> superlattices. Bulk SrVO<sub>3</sub> is a paramagnetic metal with a nominal V  $d^1$  occupancy, while bulk SrMnO<sub>3</sub> is an antiferromagnetic insulator with a nominal Mn  $d^3$  occupancy. In the SrVO<sub>3</sub>/SrMnO<sub>3</sub> superlattice, the partially occupied V  $t_{2g}$  states have similar energy to the empty Mn  $e_g$  states, which results in an incomplete charge transfer, i.e. nominally the valence of V changes from 4 to  $(4 + x)$  and the valence of Mn changes from 4 to  $(4 - x)$  where  $0 < x < 1$ . Figure 14 shows the theoretically calculated spectral functions of bulk SrMnO<sub>3</sub>, SrVO<sub>3</sub> and (SrMnO<sub>3</sub>)<sub>1</sub>/(SrVO<sub>3</sub>)<sub>1</sub> superlattice. All the calculations are performed in paramagnetic states. Figure 14(A) shows that a Mott gap is opened in bulk SrMnO<sub>3</sub>. Figure 14(B) shows that bulk SrVO<sub>3</sub> is paramagnetic metallic with V  $t_{2g}$  states at the Fermi surface. The panels (C) of figure 14 show the

spectral function of (SrMnO<sub>3</sub>)<sub>1</sub>/(SrVO<sub>3</sub>)<sub>1</sub> superlattice. In Figure 14(C1) the Mn  $e_g$  states are partially occupied, which leads to emergent metallic behavior on Mn atoms in the superlattice. In figure 14(C2) the V  $t_{2g}$  states are still partially occupied instead of empty, indicating that nominally less than one complete electron is transferred from V to Mn, in contrast to the complete charge transfer in (LaTiO<sub>3</sub>)<sub>1</sub>/(LaNiO<sub>3</sub>)<sub>1</sub> superlattice. Furthermore, since SrMnO<sub>3</sub> is electron doped, the double exchange mechanism favors a ferromagnetic ordering, just as in La<sub>1-x</sub>Sr<sub>x</sub>MnO<sub>3</sub> [45]. In the (SrVO<sub>3</sub>)<sub>1</sub>/(SrMnO<sub>3</sub>)<sub>1</sub> superlattice, ferromagnetism is expected to emerge in the MnO<sub>2</sub> layer.

A closely related oxide heterostructure is Sr<sub>2</sub>VO<sub>4</sub>/Sr<sub>2</sub>MnO<sub>4</sub> superlattice [72]. In this 214 Ruddlesden-Popper superlattice, similar charge transfer phenomenon from V to Mn occurs like the counterpart SrVO<sub>3</sub>/SrMnO<sub>3</sub> superlattice. Synthesizing transition metal oxides of a complicated Ruddlesden-Popper structure is now feasible in experiment [73]. Designing Ruddlesden-Popper superlattices is an interesting direction for future research.

### 5.6. Manganite/cuprate interfaces

Partial charge transfer also occurs to the interface between the ferromagnetic conducting manganite La<sub>2/3</sub>Ca<sub>1/3</sub>MnO<sub>3</sub> and the superconducting cuprate YBa<sub>2</sub>Cu<sub>3</sub>O<sub>7</sub>. The atomic structure of the interface is shown in figure 15(A). It is more complicated than the AMO<sub>3</sub>/AM'O<sub>3</sub> superlattices, but the underlying charge transfer can be understood in a similar way to the previous examples we have reviewed.

In [74], the authors observe a  $0.2e$  charge transfer from Mn to Cu per ion pair across the interface between La<sub>2/3</sub>Ca<sub>1/3</sub>MnO<sub>3</sub> and YBa<sub>2</sub>Cu<sub>3</sub>O<sub>7</sub>. The direction of charge transfer can be deduced from our simple schematics of figure 5 that with respect to  $O-p$  states, Mn- $d$  state lie above Cu- $d$  states. Figure 15(B) shows a detailed analysis of charge transfer at the interface. In theory, the on-site energy on Mn can be considered as a tuning parameter to control the charge transfer. In the right inset of figure 15(B) the energy of Mn  $d_{3z^2-r^2}$  has the same energy as that of Cu  $d_{3z^2-r^2}$  and the hole resides on Cu  $d_{x^2-y^2}$  orbital. In the left inset of figure 15(B) as the energy of Mn  $d_{3z^2-r^2}$  increases, a partial charge transfer occurs from Mn to Cu. In addition, the antibonding state formed by Cu  $d_{3z^2-r^2}$  and Mn  $d_{3z^2-r^2}$  orbitals has higher energy than that of Cu  $d_{x^2-y^2}$  orbital. Therefore the hole on Cu atoms moves from  $d_{x^2-y^2}$  to  $d_{3z^2-r^2}$  orbitals. In [75], at the same interface, the authors also find significant re-arrangement of magnetic domain structures accompanying charge transfer from Mn to Cu atoms.

### 5.7. Antisite defects

In this section, we discuss antisite defects at oxide interfaces, which turn out to have close connections to charge transfer [67, 76]. Antisite defects in which atoms exchange places across an interface may be important. Here we focus on one particular type of antisite defects: at the interface between two semi-infinite perovskite oxides, two  $B$ -site transition metal

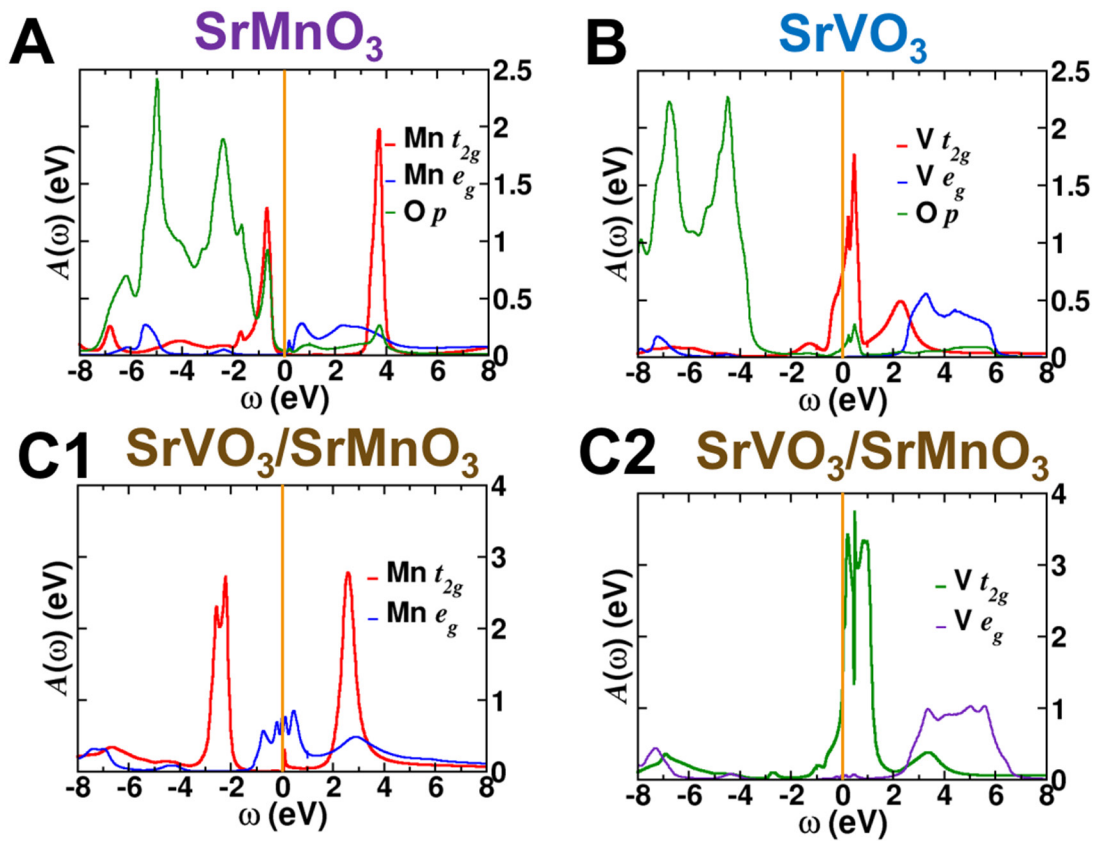


**Figure 14.** (A) Spectral function of cubic SrMnO<sub>3</sub>. The red, blue and green are Mn-*t*<sub>2g</sub>, Mn-*e*<sub>g</sub> and O-*p* projected densities of states, respectively. (B) Spectral function of cubic SrVO<sub>3</sub>. The red, blue and green are V-*t*<sub>2g</sub>, V-*e*<sub>g</sub> and O-*p* projected densities of states, respectively. (C1) Spectral function of SrVO<sub>3</sub>/SrMnO<sub>3</sub> superlattices. The red and blue curves are Mn-*t*<sub>2g</sub> and Mn-*e*<sub>g</sub> projected densities of states. (C2) Spectral function of SrVO<sub>3</sub>/SrMnO<sub>3</sub> superlattices. The green and purple curves are V-*t*<sub>2g</sub> and V-*e*<sub>g</sub> projected densities of states. Adapted with permission from [72]. Copyright (2014) by the American Physical Society.

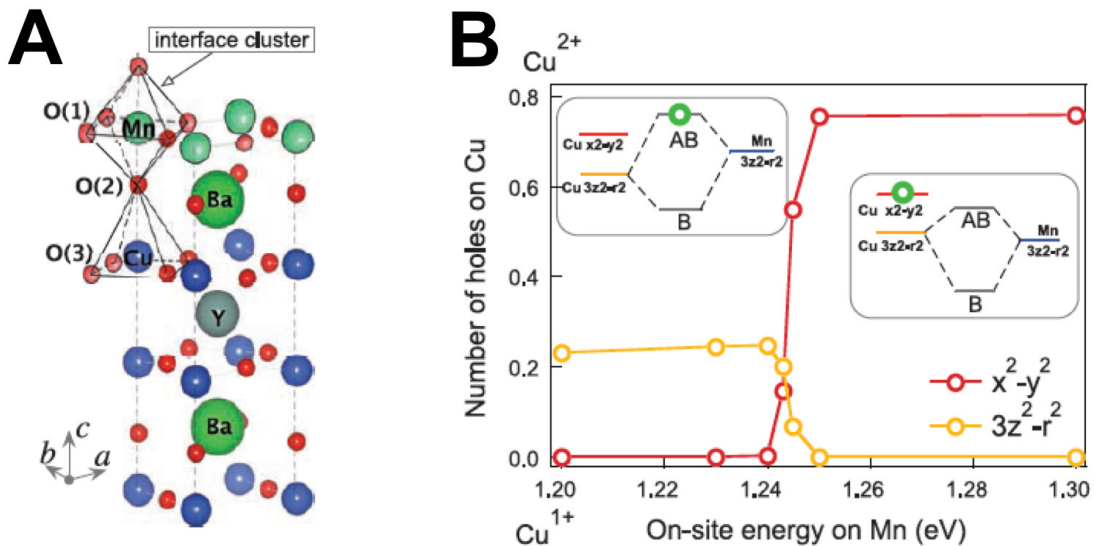


**Figure 15.** (A) Atomic positions near the La<sub>2/3</sub>Ca<sub>1/3</sub>MnO<sub>3</sub>/YBa<sub>2</sub>Cu<sub>3</sub>O<sub>7</sub> (LCMO/YBCO) interface. The MnCuO<sub>10</sub> cluster used for the exact-diagonalization calculations is highlighted. (B) Occupancy of Cu *d* orbitals at the LCMO/YBCO interface as a function of Mn hole on-site energy, as predicted by the exact-diagonalization calculations described in the text. The occupancy is given by the total number of holes, measured from the full-shell (*3d*<sup>10</sup>) electron configuration. The corresponding formal Cu valence states are indicated for clarity. The insets show the orbital level scheme at the interface, including extended bonding (B) and antibonding (AB) ‘molecular orbitals’ formed by hybridized Cu and Mn *d*<sub>3z<sup>2</sup>-r<sup>2</sup> orbitals. The hole is indicated as the green circle. From [74]. Reprinted with permission from AAAS.</sub>

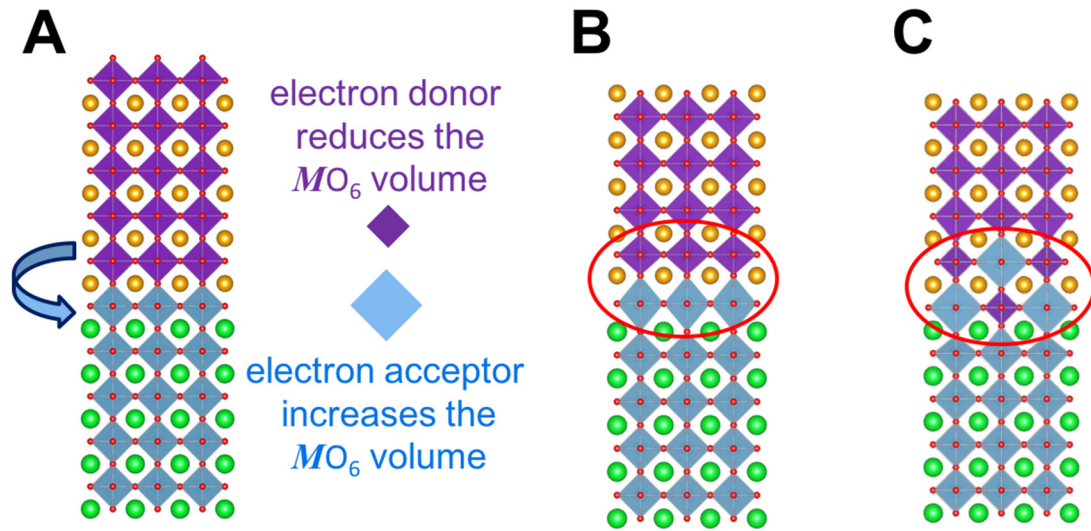


**Figure 16.** (A) Atomic structure of an interface between two semi-infinite perovskite oxides. The arrow indicates a charge transfer. After the charge transfer, the electron donor has a smaller  $MO_6$  oxygen octahedron, while the electron acceptor has a larger  $MO_6$  oxygen octahedron. Here  $M$  is a transition metal. (B) Atomic structure of an ideal interface with substantial charge transfer across the interface. The  $MO_6$  oxygen octahedron of electron donor is under tensile strain. The  $MO_6$  oxygen octahedron of electron acceptor is under compressive strain. (C) Atomic structure of an interface with substantial charge transfer across the interface and antisite defects. The volume disproportionation of oxygen octahedron  $MO_6$  between electron donor and electron acceptor is naturally accommodated by antisite defects.

ions interchange their positions. As figure 16(A) shows, if substantial charge transfer occurs across the interface, the  $BO_6$  oxygen octahedron that donates the electron shrinks its volume, while the  $B'O_6$  oxygen octahedron that accepts the electron expands its volume. If the interface remains atomically sharp as in figure 16(B) some  $BO_6$  oxygen octahedra (electron donors) are under tensile strain, while other  $B'O_6$  oxygen octahedra (electron acceptors) are under compressive strain. However, if antisite defects are induced at the interface (see figure 16(C)), the volume disproportionation will be naturally accommodated, which thus significantly reduces the internal strain. This indicates that significant charge transfer across oxide interfaces is a fundamental thermodynamic driving force to induce antisite defects.

In [67], the authors use first-principles methods to survey 21  $LaMO_3/LaM'O_3$  interfaces ( $M, M' = Ti, V, Cr, Mn, Fe, Co, Ni$ ) and 15  $SrMO_3/SrM'O_3$  interfaces ( $M, M' = Ti, V, Cr, Mn, Fe, Co$ ). The authors find that about 50% of the surveyed interfaces have strong tendency for antisite defects and these interfaces have a high degree of charge transfer between two dissimilar transition metal ions.

Chen and Millis [67] also show that for interfaces with negligible charge transfer, the presence of Jahn–Teller distortions can help inhibit antisite defects. Figure 17 shows the effects of Jahn–Teller distortions at oxide interfaces. Panel (A) shows the top view of two vertically adjacent oxide layers at the interface with no antisite defects. The purple oxygen octahedron has strong Jahn–Teller distortions (one long metal–oxygen bond length and one short metal–oxygen bond length). The blue oxygen octahedron has no Jahn–Teller distortions (two metal–oxygen bond lengths are equal). Panel (B) shows the top view of two vertical adjacent oxide layers at the interface with one antisite defect. The purple oxygen octahedron has bond disproportionation (Jahn–Teller distortion) and the blue oxygen octahedron does not have bond disproportionation. Compatibility

with the geometry imposes strains (green arrows) to reduce the bond disproportionation of the purple oxygen octahedron and to induce a bond disproportionation in the blue oxygen octahedron. To reduce the elastic strain, the ideal interface with no antisite defects is thermodynamically favored.

We summarize that antisite defects are strongly associated with geometry constraints, which in turn are controlled by the charge states of transition metal ions and are therefore closely connected to charge transfer. Antisite defects are favored at oxide interfaces if the defect allows the system to accommodate volume disproportionation induced by charge transfer. On the other hand, if the ideal (un-defected) interface can accommodate bond disproportionation due to Jahn–Teller distortions (perhaps also due to charge transfer), antisite defects are disfavored.

## 6. Theoretical challenges

In this section, we briefly review the theoretical methods that are used to calculate oxide heterostructures and discuss the challenges faced in order to better understand charge-transfer-driven phenomena at oxide interfaces.

The key quantities to calculate are the band alignments between occupied and unoccupied states in bulk materials and between similar states on opposite sides of an interface. Therefore, the biggest challenge is to develop a method with no fitting parameters that calculates electronic structure of realistic materials (including complex heterostructures).

Currently, density functional theory (DFT) [77, 78] with local density approximation (LDA) [79] and generalized gradient approximation (GGA) [80] is the workhorse to calculate the crystal structure of oxide heterostructures. Because this method gives access to the energy as a function of atomic positions, it can capture complicated distortions in oxides, including oxygen octahedral rotations, ferroelectric displacements

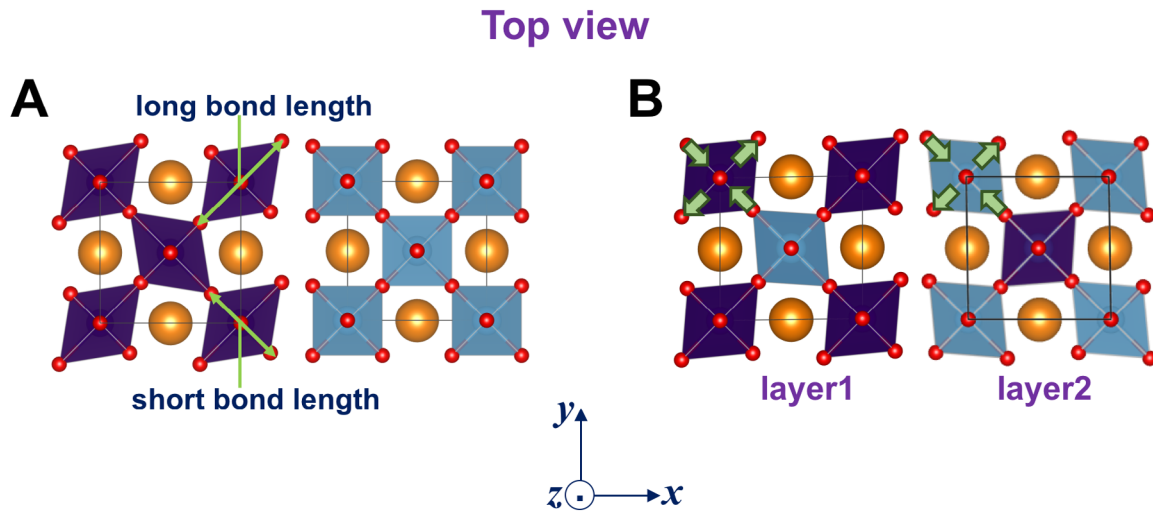


**Figure 17.** (A) Top view of two vertically adjacent oxide layers at the interface with no antisite defects. The purple oxygen octahedron has strong Jahn–Teller distortions (one long metal–oxygen bond length and one short metal–oxygen bond length). The blue oxygen octahedron has no Jahn–Teller distortions (two metal–oxygen bond lengths are equal). (B) Top view of two vertical adjacent oxide layers at the interface with one antisite defect. The purple oxygen octahedron has bond disproportionation (Jahn–Teller distortion) and the blue oxygen octahedron does not have bond disproportionation. Compatibility with the geometry imposes strains (green arrows) to reduce the bond disproportionation of the purple oxygen octahedron and to induce a disproportionation in the blue oxygen octahedron. Rotations and tilts of oxygen octahedra are suppressed for clarity. Adapted with permission from [67]. Copyright (2016) by the American Physical Society.

and metal–oxygen bond disproportionation. However, DFT is a ground state theory which (with the exact exchange correlation functional) yields the correct ground state energy, its charge density and crystal structure (after atomic relaxation). The DFT-calculated electronic structure (band structure and density of state) that is based on fictitious Kohn–Sham orbitals is in principle unphysical and therefore band alignment need not be correct. In practice, for weakly correlated materials such as band insulators, the DFT-calculated electronic structure is qualitatively reasonable, but quantitatively it underestimates the size of band gaps by 30–50%. However, for strongly correlated materials including transition metal oxides, the DFT-calculated electronic structure can be qualitatively incorrect (DFT predicts a metallic ground state for various Mott insulators). Since DFT can not accurately calculate energy separation between metal  $d$  and oxygen  $p$  states in many strongly correlated oxides, in oxide heterostructures DFT can also make incorrect predictions on the band alignment of  $d$  states between two different transition metal atoms, which is the key variable to control charge transfer phenomena.

In order to improve the electronic structure calculated by DFT, various extensions and more sophisticated many-body theory methods have been used in literature. One of the most widely used extension is DFT plus Hubbard  $U$  and Hund’s  $J$  corrections, commonly known as the DFT +  $U$  method [81, 82]. In this method, the correlation effects are treated in a static mean-field approximation. The biggest advantage of this method is that its computational scaling is almost the same as standard DFT calculations and atomic relaxation can be performed within the method. However, Hubbard  $U$  and Hund’s  $J$  are element-dependent and are fixed phenomenologically. More importantly, DFT +  $U$  method is a static mean field approximation that can not describe many important dynamical correlated phenomena, such as the Mott insulating state. DFT plus dynamical mean field theory (DFT+DMFT)

is another major extension of DFT [83, 84]. In DFT+DMFT method, DFT calculates the hopping matrix elements of the underlying lattice model for realistic materials, while single-site DMFT calculates a frequency-dependent self energy and the corresponding spectral functions. DFT+DMFT method can describe many dynamical correlated phenomena, such as Mott state and correlation-driven band reduction. More importantly, if Hubbard  $U$  and Hund’s  $J$  parameters are correct, the band alignment based on the DMFT-calculated spectral functions is more accurate and reliable than that based on the DFT-calculated density of states. However, like DFT +  $U$ , DFT+DMFT method itself does not calculate the element-dependent  $U$  and  $J$ . Furthermore, the calculation of forces on atoms in complex solids within the DMFT method is still in infancy [11, 85, 86]. Therefore unlike DFT +  $U$  method, atomic relaxation is not feasible in DFT+DMFT method at this stage. Another important issue in both DFT +  $U$  and DFT+DMFT is the double counting problem. In both methods, the separation of DFT and extension raises the possibility that some interactions will be included in both parts and will therefore be counted twice, necessitating the subtraction of an additional double counting term. The physical properties calculated from DFT +  $U$  or DFT+DMFT sensitively depend on double counting, but unfortunately the exact form of double counting is unknown. In literature a widely used empirical double counting form is called fully localized limit (FLL) [87]. However, recent work [88] shows that the FLL double counting may lead to an inaccurate energy separation between metal  $d$  and oxygen  $p$  states in rare earth nickelates. However, how to improve the FLL counting in DFT +  $U$  and DFT+DMFT calculations is one of the biggest theoretical challenges of the methods.

Another two methods-hybrid functional [89] and GW [90]-have also been used in literature to calculate the electronic structure of complex oxides as an improvement over

**Table 1.** Table of different charge transfer mechanisms in oxide heterostructures. For each mechanism, representative examples with the corresponding emergent phenomena are provided.

Mechanisms	Examples	Emergent phenomena
Polarity difference	LaAlO <sub>3</sub> /SrTiO <sub>3</sub>	The interface is metallic, magnetic and superconducting, although the constituents are insulators in bulk.
Occupancy difference	LaTiO <sub>3</sub> /SrTiO <sub>3</sub>	The interface is metallic, although LaTiO <sub>3</sub> is a Mott insulator and SrTiO <sub>3</sub> is a band insulator.
Electro-negativity difference	LaTiO <sub>3</sub> /LaNiO <sub>3</sub>	Ni at the interface is in a $d^8$ Mott insulating state, although Ni in LaNiO <sub>3</sub> is in a $d^7$ metallic state.
	LaTiO <sub>3</sub> /LaNiO <sub>3</sub> / LaAlO <sub>3</sub>	Ni at the interface has a huge orbital polarization, although Ni in LaNiO <sub>3</sub> has a negligible orbital polarization.
	LaMnO <sub>3</sub> /LaNiO <sub>3</sub>	The interface can be either insulating or metallic depending on the thickness of LaMnO <sub>3</sub> and LaNiO <sub>3</sub> , although LaMnO <sub>3</sub> is an insulator and LaNiO <sub>3</sub> is a metal.
	Ba <sub>2</sub> VFeO <sub>6</sub>	Ba <sub>2</sub> VFeO <sub>6</sub> is ferroelectric although both BaVO <sub>3</sub> and BaFeO <sub>3</sub> have cubic structures (not ferroelectric).
	SrVO <sub>3</sub> /SrMnO <sub>3</sub>	Mn at the interface is doped and becomes metallic although SrMnO <sub>3</sub> is an insulator.
	Manganite /cuprate	At the interface the Cu has a multi-orbital Fermi surface, although it is single-band in bulk; and the Mn forms different magnetic domain structures from bulk.

DFT. The advantage of both methods is that they do not involve material-dependent parameters but both methods are very computationally intensive. Therefore the calculations using both methods are constrained to small systems and atomic relaxation is not practically feasible for complex heterostructures.

We note that in many strongly correlated materials, electronic structure and atomic structure are closely related. For example, VO<sub>2</sub> undergoes a coupled metal-insulator rutile-monoclinic transition [91, 92]. While it is still an on-going research topic whether the transition is primarily driven by electronic transition or structural transition, it is a classical example for strongly correlated materials that different atomic structures correspond to distinct electronic structures. For oxide heterostructures, atoms close to the interface generically move away from their positions in bulk constituents and charge transfer phenomenon is strongly coupled to the new atomic positions because they can significantly change the energy separation between metal  $d$  states and oxygen  $p$  states as well as hopping matrix elements and band widths [67]. Currently DFT and DFT +  $U$  methods can efficiently calculate forces on atoms in solids and therefore can perform atomic relaxation and obtain optimal atomic positions for complex heterostructures. However, strong correlation effects are either neglected in DFT or treated in a static mean field approximation in DFT +  $U$ . On the other hand, DMFT/hybrid functional/GW improve the calculations of electronic structure to different extent, but atomic relaxation is very difficult, if not possible, using these sophisticated methods. The compromising approach of using DFT/DFT +  $U$  to obtain the optimal atomic structure or simply using experimentally determined atomic structure, and then using DMFT/hybrid functional/GW methods to calculate electronic structure is currently preferred. A unified theory which can calculate both electronic and atomic structures for strongly correlated materials on the same footing is highly desirable but very challenging. We finally note that while the calculation of many-body band offsets is a key theoretical challenge, measurements of charge transfer and band offsets in experiment can provide a key test of theories.

## 7. Summary and perspectives

We reviewed three major mechanisms for charge transfer in oxide heterostructures. In our classification, charge transfer can occur across oxide interfaces in order to compensate for (1) polarity difference, (2) occupancy difference and (3) electronegativity difference between two different transition metal oxides. We summarized representative examples for the first two mechanisms and present a more detailed review of important examples for the third mechanism. Table 1 provides a quick summary. We also reviewed the theoretical methods used to study charge transfer phenomena in oxide heterostructures and discuss the challenges we face in theory.

Oxide heterostructures have shown a plethora of properties which are not exhibited in their bulk constituents. Charge transfer is a very general and robust phenomenon that occurs to oxide interfaces. In the review, we highlight oxide interfaces in which charge transfer occurs to  $3d$  transition metal ions. However, recent experimental progress makes it feasible to synthesize oxide heterostructures that contain  $4d$  and  $5d$  transition metal ions [93]. Charge transfer between  $3d$ -to- $4d$  or  $3d$ -to- $5d$  transition metal ions is a very interesting direction for future research, since spin-orbit interaction is stronger in  $4d$  and  $5d$  transition metal ions and the interplay between correlation effects and spin-orbit interaction will play a crucial role in charge transfer phenomena. While our review mainly focuses on (001) interfaces, the emergent phenomena identified in oxide heterostructures may also be present in mixed bulk materials, such as double perovskite oxides (e.g. see section 5 (D)). We hope our review can stimulate further theoretical and experimental work to search for novel strongly correlated phenomena in oxide heterostructures.

## Acknowledgments

We are grateful to useful discussion with M Bibes, H T Dang, S Dong, A Georges, M Gibert, C Marianetti, H Park, K Shen, D Schlom, Z Zhong and in particular S Ismail-Beigi. H Chen is supported by National Science Foundation under Grant No. DMR-1120296. A J Millis is supported by the

Department of Energy under Grant No. DOE-ER-046169. Computational facilities are provided via Extreme Science and Engineering Discovery Environment (XSEDE), which is supported by National Science Foundation through Grant No. ACI-1548562 and also via the National Energy Research Scientific Computing Center (NERSC), a DOE Office of Science User Facility supported by the Office of Science of the US Department of Energy.

## References

- [1] Hwang H, Iwasa Y, Kawasaki M, Keimer B, Nagaosa N and Tokura Y 2012 *Nat. Mater.* **11** 103
- [2] Ohtomo A and Hwang H Y 2004 *Nature* **427** 423
- [3] Thiel M J, Hammerl G S, Schmehl A and Schneider C W 2006 *Science* **313** 1942
- [4] Reyren N *et al* 2007 *Science* **317** 1196
- [5] Brinkman A, Huijben M, van Zalk M, Huijben J, Zeitler U, Maan J C, van der Wiel W G, Rijnders G, Blank D H A and Hilgenkamp H 2007 *Nat. Mater.* **6** 493
- [6] Caviglia A D, Gariglio S, Reyren N, Jaccard D, Schneider T, Gabay M, Thiel S, Hammerl G, Mannhart J and Triscone J-M 2008 *Nature* **456** 624
- [7] Li L, Richter C, Mannhart J and Ashoori R C 2011 *Nat. Phys.* **7** 762
- [8] Bert J A, Kalisky B, Bell C, Kim M, Hikita Y, Hwang H Y and Moler K A 2011 *Nat. Phys.* **7** 767
- [9] Tokura Y and Hwang H Y 2008 *Nat. Mater.* **7** 694
- [10] Zubko P, Gariglio S, Gabay M, Ghosez P and Triscone J-M 2011 *Annu. Rev. Condens. Matter Phys.* **2** 141
- [11] Chakhalian J, Freeland J W, Millis A J, Panagopoulos C and Rondinelli J M 2014 *Rev. Mod. Phys.* **86** 1189
- [12] Huijben M, Brinkman A, Koster G, Rijnders G, Hilgenkamp H and Blank D H A 2009 *Adv. Mater.* **21** 1665
- [13] Chen H, Kolpak A and Ismail-Beigi S 2010 *Adv. Mater.* **22** 2881
- [14] Pentcheva R and Pickett W E 2010 *J. Phys.: Condens. Matter* **22** 043001
- [15] Shi Y *et al* 2013 *Nat. Mater.* **12** 1024
- [16] Kim T H *et al* 2016 *Nature* **533** 68
- [17] Chen H, Kolpak A and Ismail-Beigi S 2010 *Phys. Rev. B* **82** 085430
- [18] Millis A J and Schlom D G 2010 *Phys. Rev. B* **82** 073101
- [19] Mannhart J, Blank D H A, Hwang H Y, Millis A J and Triscone J-M 2008 *MRS Bull.* **33** 1027
- [20] Zaanen J, Sawatzky G A and Allen J W 1985 *Phys. Rev. Lett.* **55** 418
- [21] Nakagawa N, Hwang H Y and Muller D A 2006 *Nat. Mater.* **5** 204
- [22] Caviglia A D, Gabay M, Gariglio S, Reyren N, Cancellieri C and Triscone J M 2010 *Phys. Rev. Lett.* **104** 126803
- [23] Lesne E *et al* 2016 *Nat. Mater.* **15** 1261–6
- [24] Segal Y, Ngai J H, Reiner J W, Walker F J and Ahn C H 2009 *Phys. Rev. B* **80** 241107
- [25] Singh-Bhalla G, Bell C, Ravichandran J, Siemons W, Hikita Y, Salahuddin S, Hebard A F, Hwang H Y and Ramesh R 2011 *Nat. Phys.* **7** 80
- [26] Chen H, Kolpak A and Ismail-Beigi S 2009 *Phys. Rev. B* **79** 161402
- [27] Yu L and Zunger A 2014 *Nat. Commun.* **5** 5118
- [28] Chambers S A, Qiao L, Droubay T C, Kaspar T C, Arey B W and Sushko P V 2011 *Phys. Rev. Lett.* **107** 206802
- [29] Ohtomo A, Muller D A, Grazul J L and Hwang H Y 2002 *Nature* **419** 378
- [30] Okamoto S and Millis A J 2004 *Nature* **428** 630
- [31] Monkman E J, Adamo C, Mundy J A, Shai D E, Harter J W, Shen D, Burganov B, Muller D A, Schlom D G and Shen K M 2012 *Nat. Mater.* **11** 855
- [32] May S J *et al* 2009 *Nat. Mater.* **8** 892
- [33] Lüders U, Sheets W C, David A, Prellier W and Frésard 2009 *Phys. Rev. B* **80** 241102
- [34] Dang H T and Millis A J 2013 *Phys. Rev. B* **87** 184434
- [35] Moetakef P, Cain T A, Ouellette D G, Zhang J Y, Klenov D O, Janotti A, Van de Walle C G, Rajan S, Allen S J and Stemmer S 2011 *Appl. Phys. Lett.* **99** 232116
- [36] Jang H W *et al* 2011 *Science* **331** 886
- [37] Moetakef P, Jackson C A, Hwang J, Balents L, Allen S J and Stemmer S 2012 *Phys. Rev. B* **86** 201102
- [38] Chen R, Lee S and Balents L 2013 *Phys. Rev. B* **87** 161119
- [39] Smadici S, Abbamonte P, Bhattacharya A, Zhai X, Jiang B, Rusydi A, Eckstein J N, Bader S D and Zuo J M 2007 *Phys. Rev. Lett.* **99** 196404
- [40] Bhattacharya A, May S J, Te Velthuis S G E, Warusawithana M, Zhai X, Jiang B, Zuo J M, Fitzsimmons M R, Bader S D and Eckstein J N 2008 *Phys. Rev. Lett.* **100** 257203
- [41] Dong S, Yu R, Yunoki S, Alvarez G, Liu J M and Dagotto E 2008 *Phys. Rev. B* **78** 201102
- [42] Nanda B R K and Satpathy S 2009 *Phys. Rev. B* **79** 054428
- [43] Dang H T and Millis A J 2013 *Phys. Rev. B* **87** 155127
- [44] Imada M 1998 *Rev. Mod. Phys.* **70** 1039
- [45] Salamon M B and Jaime M 2001 *Rev. Mod. Phys.* **73** 583
- [46] Moetakef P, Cain T A, Ouellette D G, Zhang J Y, Klenov D O, Janotti A, Van de Walle C G, Rajan S, Allen S J and Stemmer S 2011 *Appl. Phys. Lett.* **99** 232116
- [47] Yoshimatsu K, Okabe T, Kumigashira H, Okamoto S, Aizaki S, Fujimori A and Oshima M 2010 *Phys. Rev. Lett.* **104** 147601
- [48] Boris A V *et al* 2011 *Science* **332** 937
- [49] Stemmer S and Millis A J 2013 *MRS Bull.* **38** 1032
- [50] Chen H, Millis A and Marianetti C 2013 *Phys. Rev. Lett.* **111** 116403
- [51] Cao Y, Liu X, Kareev M, Choudhury D, Middey S, Meyers D, Kim J W, Ryan P, Freeland J W and Chakhalian J 2016 *Nat. Commun.* **7** 10418
- [52] Grisolia M N *et al* 2016 *Nat. Phys.* **12** 484
- [53] Chen H, Kumah D P, Disa A S, Walker F J, Ahn C H and Ismail-Beigi S 2013 *Phys. Rev. Lett.* **110** 186402
- [54] Chaloupka J and Khaliullin G 2008 *Phys. Rev. Lett.* **100** 016404
- [55] Hansmann P, Yang X, Toschi A, Khaliullin G, Andersen O K and Held K 2009 *Phys. Rev. Lett.* **103** 016401
- [56] Disa A, Kumah D, Malashevich A, Chen H, Arena D, Specht E, Ismail-Beigi S, Walker F and Ahn C 2015 *Phys. Rev. Lett.* **114** 026801
- [57] Fabbris G *et al* 2016 *Phys. Rev. Lett.* **117** 147401
- [58] Kleibeuker J E *et al* 2014 *Phys. Rev. Lett.* **113** 237402
- [59] Zhang H, Weng Y, Yao X and Dong S 2015 *Phys. Rev. B* **91** 195145
- [60] Zhong Z and Hansmann P 2017 *Phys. Rev. X* **7** 011023
- [61] Hoffman J, Tung I C, Nelson-Cheeseman B B, Liu M, Freeland J W and Bhattacharya A 2013 *Phys. Rev. B* **88** 144411
- [62] Di Pietro P, Hoffman J, Bhattacharya A, Lupi S and Perucchi A 2015 *Phys. Rev. Lett.* **114** 156801
- [63] Lee A T and Han M J 2013 *Phys. Rev. B* **88** 035126
- [64] Das H, Waghmare U V, Saha-Dasgupta T and Sarma D D 2008 *Phys. Rev. Lett.* **100** 186402
- [65] Singh M P, Truong K D and Fournier P 2007 *Appl. Phys. Lett.* **91** 042504
- [66] Singh M P, Truong K D, Jandl S and Fournier P 2009 *Phys. Rev. B* **79** 224421
- [67] Chen H and Millis A 2016 *Phys. Rev. B* **93** 104111

- [68] Gibert M, Zubko P, Scherwitzl R, Íniguez J and Triscone J-M 2012 *Nat. Mater.* **11** 195
- [69] Gibert M, Viret M, Zubko P, Jaouen N, Tonnerre J-M, Torres-Pardo A, Catalano S, Gloter A, Stéphan O and Triscone J-M 2016 *Nat. Commun.* **7** 11227
- [70] Wu X, Rabe K M and Vanderbilt D 2011 *Phys. Rev. B* **83** 020104
- [71] Chen H and Millis A J 2017 submitted
- [72] Chen H, Park H, Millis A and Marianetti C 2014 *Phys. Rev. B* **90** 245138
- [73] Lee C-H *et al* 2013 *Nature* **502** 532
- [74] Chakhalian J, Freeland J W, Habermeier H-U, Cristiani G, Khaliullin G, van Veenendaal M and Keimer B 2007 *Science* **318** 1114
- [75] Chakhalian J *et al* 2006 *Nat. Phys.* **2** 244
- [76] Neumann R F, Bahiana M and Binggeli N 2012 *Europhys. Lett.* **100** 67002
- [77] Hohenberg P and Kohn W 1964 *Phys. Rev.* **136** B864
- [78] Kohn W and Sham L J 1965 *Phys. Rev.* **140** A1133
- [79] Perdew J P and Zunger A 1981 *Phys. Rev. B* **23** 5048
- [80] Perdew J P, Burke K and Ernzerhof M 1996 *Phys. Rev. Lett.* **77** 3865
- [81] Liechtenstein A I, Anisimov V I and Zaanen J 1995 *Phys. Rev. B* **52** R5467
- [82] Dudarev S, Botton G, Savrasov S, Humphreys C and Sutton A 1998 *Phys. Rev. B* **57** 1505
- [83] Georges A, Kotliar G, Krauth W and Rozenberg M J 1996 *Rev. Mod. Phys.* **68** 13
- [84] Kotliar G, Savrasov S Y, Haule K, Oudovenko V S, Parcollet O and Marianetti C A 2006 *Rev. Mod. Phys.* **78** 865
- [85] Leonov I, Anisimov V I and Vollhardt D 2014 *Phys. Rev. Lett.* **112** 146401
- [86] Haule K and Pascut G L 2016 *Phys. Rev. B* **94** 195146
- [87] Czyżyk M T and Sawatzky G A 1994 *Phys. Rev. B* **49** 14211
- [88] Park H, Millis A J and Marianetti C A 2014 *Phys. Rev. B* **89** 245133
- [89] Kümmel S and Kronik L 2008 *Rev. Mod. Phys.* **80** 3
- [90] Hedin L 1965 *Phys. Rev.* **139** A796
- [91] Morin F J 1959 *Phys. Rev. Lett.* **3** 34
- [92] Barker A S, Verleur H W and Guggenheim H J 1966 *Phys. Rev. Lett.* **17** 1286
- [93] Matsuno J, Ihara K, Yamamura S, Wadati H, Ishii K, Shankar V V, Kee H-Y and Takagi H 2015 *Phys. Rev. Lett.* **114** 247209